

# The CARMA-NRO Orion Survey: Protostellar Outflows, Energetics, and Filamentary Alignment

Jesse R. Feddersen 10, Héctor G. Arce 10, Shuo Kong 10, Sümeyye Suri 2, Álvaro Sánchez-Monge 2, Volker Ossenkopf-Okada 20, Michael M. Dunham 30, Fumitaka Nakamura 40, Yoshito Shimajiri 50, and John Bally 60

Department of Astronomy, Yale University, P.O. Box 208101, New Haven, CT 06520-8101, USA; jesse.feddersen@yale.edu

1. Physikalisches Institut, Universität zu Köln, Zülpicher Str. 77, D-50937 Köln, Germany

Department of Physics, State University of New York at Fredonia, 280 Central Avenue, Fredonia, NY 14063, USA

4 National Astronomical Observatory of Japan, 2-21-1 Osawa, Mitaka, Tokyo 181-8588, Japan

5 Laboratoire AIM, CEA/DSM-CNRS-Université Paris Diderot, IRFU/Service dAstrophysique, CEA Saclay, F-91191 Gif-sur-Yvette, France

6 Department of Astrophysical and Planetary Sciences, University of Colorado, Boulder, CO, USA

Received 2019 October 22; revised 2020 April 3; accepted 2020 April 3; published 2020 June 8

#### **Abstract**

We identify 45 protostellar outflows in CO maps of the Orion A giant molecular cloud from the Combined Array for Research in Millimeter-wave Astronomy–Nobeyama Radio Observatory Orion survey. Our sample includes 11 newly detected outflows. We measure the mass and energetics of the outflows, including material at low velocities, by correcting for cloud contributions. The total momentum and kinetic energy injection rates of outflows are comparable to the turbulent dissipation rate of the cloud. We also compare the outflow position angles to the orientation of C<sup>18</sup>O filaments. We find that the full sample of outflows is consistent with being randomly oriented with respect to the filaments. A subsample of the most reliable measurements shows a moderately perpendicular outflow-filament alignment that may reflect accretion of mass across filaments and onto the protostellar cores.

*Unified Astronomy Thesaurus concepts:* Star formation (1569); Giant molecular clouds (653); Stellar feedback (1602); Protostars (1302); Interstellar medium (847); Interstellar filaments (842)

Supporting material: figure set

#### 1. Introduction

Stars form inside the densest parts of giant molecular clouds (GMCs; McKee & Ostriker 2007). Bipolar, high-velocity flows of molecular gas, called outflows, are launched from forming protostars. These structures are so ubiquitous they can be observed even when the protostar itself is unseen (Kong et al. 2019). While it is unclear how exactly outflows are launched, they likely arise from the interaction of the accretion disk with magnetic fields near the protostar (e.g., Konigl & Pudritz 2000; Shu et al. 2000; Frank et al. 2014).

Outflows have long been considered as a mechanism for sustaining turbulence and slowing star formation in GMCs (Nakamura & Li 2007; Carroll et al. 2009; Federrath 2015). Surveys of outflows have repeatedly shown that they have enough aggregate momentum and kinetic energy to significantly offset the dissipation of turbulence, especially on cluster scales (Arce et al. 2010; Nakamura et al. 2011; Plunkett et al. 2013, 2015; Li et al. 2015). More uncertain is the efficiency with which outflows inject momentum at larger scales in order to maintain the observed turbulence in GMCs (Brunt et al. 2009; Padoan et al. 2009; Carroll et al. 2010). For a comprehensive review of outflows, see Arce et al. (2007), Frank et al. (2014), and Bally (2016).

In many GMCs, most of the star formation takes place in relatively narrow, dense filaments (Arzoumanian et al. 2011; Suri et al. 2019). If the angular momentum of a growing protostar is inherited from the mass accretion onto a filament, the protostellar spin and the filament direction will be correlated (Bodenheimer 1995; André et al. 2014; Li & Klein 2019). If, however, the link between mass accretion at filament scales and protostellar scales is disrupted, e.g., by

turbulence or interaction with protostellar companions, then the protostellar spin may not be correlated with the filament orientation (Offner et al. 2016; Lee et al. 2017).

To distinguish between these scenarios, several studies have recently considered the relative orientation of outflows and filaments. Assuming that outflow direction traces the angular momentum of the protostar, a correlation between the outflow and filament direction could mean a connection between sub-AU scales, where the outflow is launched, to filaments at much larger scales. Davis et al. (2009) measured the position angle of H<sub>2</sub> outflows in the Orion A GMC and found no correlation with the large-scale, integral-shaped filament. Stephens et al. (2017) compared CO outflows with filaments extracted from Herschel dust maps in the Perseus molecular cloud and likewise found a random outflow-filament alignment. However, Kong et al. (2019) recently found a preferentially perpendicular outflow-filament alignment in the IRDC G28.37+0.07

The Orion A GMC is an ideal environment for studying protostellar outflows and their connection to filaments. At a distance of 400 pc, <sup>7</sup> it is one of the closest clouds forming both low- and high-mass stars. Following earlier outflow studies, Tanabe et al. (2019) recently carried out a systematic search of CO outflows in Orion A, which complements our study. We use the same CO data as Tanabe et al. (2019), supplemented

We adopt a distance of 400 pc throughout this paper, to be consistent with the recent parallax measurements from GAIA Data Release 2 (Großschedl et al. 2018; Kounkel et al. 2018; Kuhn et al. 2019). Tanabe et al. (2019), like most previous studies of Orion A, assume a slightly greater distance of 414 pc (Menten et al. 2007). Increasing the distance by this amount would increase mass, momentum, and kinetic energy reported here by 7%. The mass-loss rate, momentum injection rate, and kinetic energy injection rate would increase by 4%. Our conclusions are not sensitive to this uncertainty in distance.

with interferometric observations that provide greater resolving power (see Section 2). Additionally, we use different methods to identify outflows and derive their physical properties. In particular, we correct for velocity-dependent opacity and low-velocity outflow emission. We also use the C<sup>18</sup>O filament catalog from Suri et al. (2019) for an entirely new analysis of the outflow-filament connection.

In this paper, we present a study of protostellar outflows in the Combined Array for Research in Millimeter-wave Astronomy (CARMA)–Nobeyama Radio Observatory (NRO) Orion survey. In Section 2, we describe the CARMA–NRO Orion CO data and protostar catalogs. In Section 3, we describe how we search for outflows in the CO maps and present the outflow catalog. In Section 4, we calculate the physical properties of the outflows and discuss their impact on the cloud. In Section 5, we discuss the relative orientation of outflows and C¹8O filaments and compare to models for random, parallel, and perpendicular outflow-filament alignment. Finally, in Section 6, we summarize our conclusions and discuss future directions. The entire outflow catalog is presented in the Appendix.

#### 2. Observations

#### 2.1. CO Maps

The CARMA–NRO Orion survey combines interferometric observations from the CARMA with single-dish observations from the 45 m telescope at the NRO. The combination of interferometric and single-dish observations results in an unprecedented spatial dynamic range of 0.01–10 pc in the Orion A molecular cloud.

We use the  $^{12}\text{CO}(1-0)$ ,  $^{13}\text{CO}(1-0)$ , and  $^{18}\text{O}(1-0)$  data first presented in Kong et al. (2018). The  $^{12}\text{CO}$  data have a resolution of  $10'' \times 8''$  and velocity resolution of 0.25 km s $^{-1}$ . The original  $^{13}\text{CO}$  data have a resolution of  $8'' \times 6''$  and a velocity resolution of 0.22 km s $^{-1}$ , but we smooth the  $^{13}\text{CO}$  data to match the resolution of  $^{12}\text{CO}$ . The  $^{18}\text{O}$  data have a resolution of  $10'' \times 8''$  and a velocity resolution of  $0.22\,\mathrm{km\ s}^{-1}$ . We do not smooth the  $^{18}\text{O}$  data, because we use them primarily for filament identification (Section 5), nor do we directly compare them to the other lines. The area covered by the CARMA–NRO Orion survey is shown in Figure 1.

# 2.2. Source Catalogs

We primarily use the Herschel Orion Protostar Survey (HOPS; Furlan et al. 2016) to assign driving sources to outflows. The HOPS catalog is the result of Herschel PACS 70–160  $\mu$ m observations of the protostars identified in the Spitzer Orion survey by Megeath et al. (2012). Furlan et al. (2016) fit the spectral energy distribution (SED) of these 330 protostars from 1.2 to 870  $\mu$ m with models to derive a variety of protostar, disk, and envelope properties.

We also use the study of  $H_2$  outflows by Davis et al. (2009) to guide our search. Davis et al. (2009) surveyed Orion A using narrowband images of the rovibrational  $H_2$  2.122  $\mu$ m line. Their work builds on previous  $H_2$  mapping by Stanke et al. (2002). We search for outflows around the 17 sources of  $H_2$  flows that are not in the HOPS catalog. In addition to the driving sources of  $H_2$  outflows, Davis et al. (2009) catalog  $H_2$  features with no obvious driving source. We also search for the CO counterpart to the 29  $H_2$  flows without an identified source

within the CO data footprint. Davis et al. (2009) measure the proper motions of 33 flows. We use the  $H_2$  images, as well as the proper motions when available, to help assign especially difficult CO outflows to driving sources.

#### 2.3. Other Outflow Studies

Orion A has been mapped extensively in CO over the past 30 years (e.g., Bally et al. 1987; Wilson et al. 2005; Shimajiri et al. 2011; Buckle et al. 2012; Ripple et al. 2013; Berné et al. 2014). Several studies have searched for outflows in the cloud using these CO observations. In the northern part of the cloud, previous searches have identified 18 outflows along the OMC 2/3 ridge (Chini et al. 1997; Aso et al. 2000; Williams et al. 2003; Shimajiri et al. 2008, 2009; Takahashi et al. 2008). In the L1641N cluster in the southern part of the cloud, Stanke & Williams (2007) and Nakamura et al. (2012) found six outflows. In the NGC 1999 region further south, previous studies have found five outflows (Morgan et al. 1991; Moro-Martín et al. 1999; Davis et al. 2000; Choi et al. 2017).

Tanabe et al. (2019) have carried out a systematic search for outflows across the Orion A cloud, using the same single-dish NRO observations that are used in our CARMA–NRO Orion survey. They identify a total of 44 outflows across the cloud, including 17 new detections. Eleven of these are in the OMC 4/5 region where no outflows had previously been found. Although we expect our catalog to largely overlap with Tanabe et al. (2019), they use an automated outflow search procedure that may include false positives. The improved resolution of the combined CARMA–NRO Orion data allows us to search for smaller outflows, helps us disentangle outflow emission in clustered regions, and aids with matching outflows to driving sources. We describe our procedure for identifying outflows below.

# 3. Outflow Identification

We search for CO outflows around each HOPS protostar in Furlan et al. (2016) and  $H_2$  jet driving source in Davis et al. (2009). For each source, we first fit a Gaussian to the average  $^{12}\text{CO}$  spectrum in a circular region of radius 15'' centered on the source. Next, we integrate the  $^{12}\text{CO}$  emission at various velocity intervals on either side of the mean velocity. We visually inspect the contour maps of the blueshifted and redshifted emission to look for collimated structures centered on the source that are detected above  $5\sigma$  in these integrated blue- and redshifted intensity maps.

In addition to the <sup>12</sup>CO blue/red contour maps, we use NIR images from the VISTA survey (Meingast et al. 2016) and the H<sub>2</sub> outflows in Davis et al. (2009) to guide our assignment of high-velocity CO to driving sources. These ancillary data are especially useful in areas of overlapping outflows, or where outflow lobes are not detected close to the driving source. When a series of H<sub>2</sub> bow shocks or NIR nebulosity that are clearly associated with a particular source overlap a region of high-velocity CO emission, we can be more confident in the assignment of this CO outflow to its source.

Tanabe et al. (2019) automatically defines any blue or redshifted emission above  $5\sigma$  near a protostar as an outflow. By restricting our catalog to structures that have the expected morphology, or are correlated with  $H_2$  flows, we limit the risk

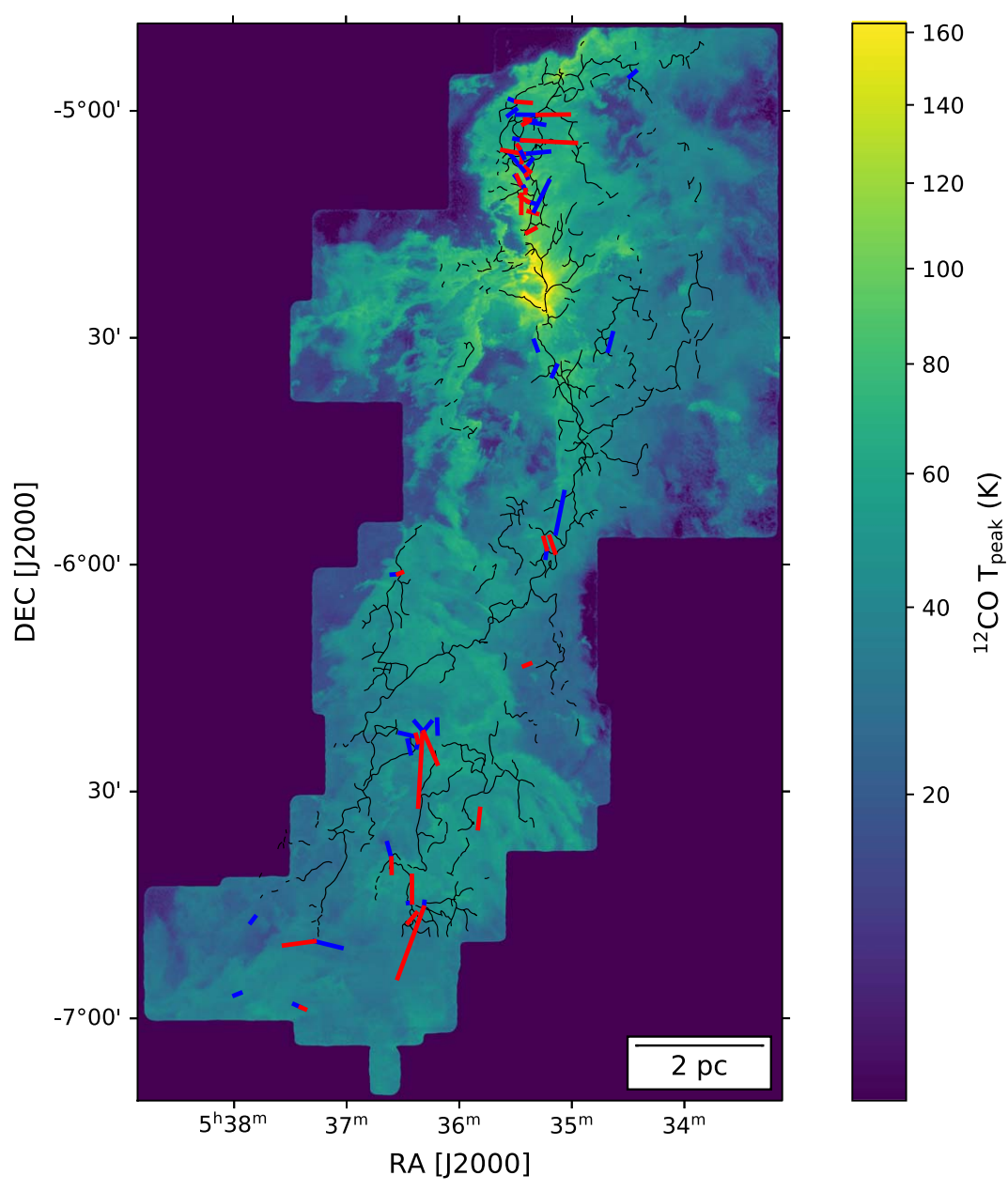


Figure 1. Peak  $^{12}$ CO antenna temperature in Orion A with outflows. The blue (red) lines indicate blue (red) outflow lobes. Length of each line denotes the maximum length of the outflow lobe,  $R_{\text{max}}$  (Section 4.1.8). Orientation of each outflow lobe indicates the measured position angle (Section 4.1.9). Black lines indicate  $C^{18}$ O filaments from Suri et al. (2019) (Section 5).

of false positives. Several of the outflows in Tanabe et al. (2019) are not included here, for that reason (see Table 1).

Some regions (e.g., OMC 2/3) contain several overlapping outflows. In these cases, we try to follow previous authors' assignment of the high-velocity emission, unless we strongly disagree with their assessment. In Section 4.1.1, we describe the outflow region extraction.

Once we have identified an outflow, we adjust the velocity range over which we integrate  $^{12}\mathrm{CO}$  to produce contour maps that most clearly separate the blue/red lobes from surrounding cloud emission. Table 1 lists these visually determined velocities,  $\nu_{\mathrm{blue}}$  and  $\nu_{\mathrm{red}}$ , which denote the lowest velocity (closest to the mean cloud velocity) where the outflow emission is clearly separated from the cloud.

For each outflow, we determine a confidence rating of "Definite" or "Marginal." Definite outflows are clearly associated

with their driving source, are clearly distinct from surrounding outflows and cloud emission, and are often clearly correlated with  $H_2$  outflows. Most definite outflows have been identified previously. Marginal outflows either have an unclear source assignment, are not clearly separated from the cloud or overlapping outflow emission, or simply are very weakly detected. In some cases, we are more confident of either the blue or red outflow lobe, so we assign confidence ratings independently to each. We expect the subset of definite outflows to have more reliable physical properties and position angles (see Section 4).

While many studies have identified energetic outflows in the OMC 1 region (e.g., Schmid-Burgk et al. 1990; Zapata et al. 2005; Teixeira et al. 2016; Bally et al. 2017), we avoid this region in our outflow search. Neither Davis et al. (2009) nor Furlan et al. (2016) cover the central part of the Orion Nebula, due to saturation and confusion with the bright nebulosity.

Table 1
Outflow Catalog

Source <sup>a</sup>	R.A.	Decl.	$v_{\text{blue}}/v_{\text{red}}^{\text{b}}$	Confidence <sup>c</sup>	Tanabe
	(J2000)	(J2000)	$(\text{km s}^{-1})$		
SMZ 11			7.5/-	M/-	9
SMZ 17	5 <sup>h</sup> 35 <sup>m</sup> 27 <sup>s</sup> 00	-5°09′54″00	3/18	D/D	
SMZ 21	5 <sup>h</sup> 35 <sup>m</sup> 26 <sup>s</sup> 90	-5°11′07″00	-/14	-/M	15
SMZ 30	5 <sup>h</sup> 35 <sup>m</sup> 18 <sup>s</sup> 30	-5°31′42″00	4.5/-	M/-	20
SMZ 50	5 <sup>h</sup> 36 <sup>m</sup> 11 <sup>s</sup> 50	$-6^{\circ}22'22''00$	4.5/-	M/-	33
HOPS 10	5 <sup>h</sup> 35 <sup>m</sup> 09 s 00	-5°58′27″48	-/12.6	-/D	27
HOPS 11	5 <sup>h</sup> 35 <sup>m</sup> 13 <sup>s</sup> 42	-5°57′57″96	4.7/12.8	$\mathrm{D}/\mathrm{D}$	26
HOPS 12	5h35m08 s 59	-5°55′54″12	4.7/-	$\mathrm{D}/-$	25
HOPS 44	5 <sup>h</sup> 35 <sup>m</sup> 10 <sup>s</sup> 58	-5°35′06″36	4.4/-	$\mathbf{M}/-$	
HOPS 50	5 <sup>h</sup> 34 <sup>m</sup> 40 <sup>s</sup> 90	-5°31′44″40	5.8/-	M/-	21
HOPS 56	5 <sup>h</sup> 35 <sup>m</sup> 19 <sup>s</sup> 46	-5°15′32″76	-/14	-/M	19
HOPS 58	5 <sup>h</sup> 35 <sup>m</sup> 18 <sup>s</sup> 50	-5°13′38″28	-/14	-/M	
HOPS 59	5 <sup>h</sup> 35 <sup>m</sup> 20 <sup>s</sup> 14	-5°13′15″60	6.9/-	$\mathbf{M}/-$	17
HOPS 60	5 <sup>h</sup> 35 <sup>m</sup> 23 <sup>s</sup> 33	-5°12′03″24	7.0/14.2	$\mathrm{D}/\mathrm{D}$	16
HOPS 68	5 <sup>h</sup> 35 <sup>m</sup> 24 <sup>s</sup> 31	-5°08′30″48	7.8/14.5	$\mathrm{D}/\mathrm{D}$	12
HOPS 70	5 <sup>h</sup> 35 <sup>m</sup> 22 <sup>s</sup> 42	-5°08′04″92	-/14	-/M	11
HOPS 71	5 <sup>h</sup> 35 <sup>m</sup> 25 <sup>s</sup> 61	-5°07′57″36	7.5/-	D/-	10
HOPS 75	5 <sup>h</sup> 35 <sup>m</sup> 26 <sup>s</sup> 66	-5°06′10″44	-/14.3	$-/\mathbf{M}$	8
HOPS 78	5 <sup>h</sup> 35 <sup>m</sup> 25 <sup>s</sup> 82	-5°05′43″80	6/15	$\mathrm{D}/\mathrm{D}$	7
HOPS 81	5 <sup>h</sup> 35 <sup>m</sup> 27 <sup>s</sup> .96	-5°04′58″08	7.5/13.5	M/M	
HOPS 84	5 <sup>h</sup> 35 <sup>m</sup> 26 <sup>s</sup> 57	-5°03′55″08	8.5/13.8	$\mathrm{D}/\mathrm{D}$	6
HOPS 87	5 <sup>h</sup> 35 <sup>m</sup> 23 <sup>s</sup> 47	-5°01′28″56	8.6/13.8	M/M	5
HOPS 88	5 <sup>h</sup> 35 <sup>m</sup> 22 <sup>s</sup> 44	-5°01′14″16	8.1/13.8	$\overline{\mathrm{D}/\mathrm{D}}$	4
HOPS 92	5 <sup>h</sup> 35 <sup>m</sup> 18 <sup>s</sup> 31	-5°00′33″12	7.6/13.7	$\mathrm{D}/\mathrm{D}$	3
HOPS 96	5 <sup>h</sup> 35 <sup>m</sup> 29 <sup>s</sup> .71	-4°58′48″72	9.8/13.9	$\mathrm{D}/\mathrm{D}$	1
HOPS 99	5 <sup>h</sup> 34 <sup>m</sup> 29 <sup>s</sup> 50	-4°55′30″72	8.3/-	$\dot{\mathrm{M}/-}$	
HOPS 157	5 <sup>h</sup> 37 <sup>m</sup> 56 <sup>s</sup> 57	-6°56′39″12	3.5/-	$\dot{\mathrm{M}/-}$	
HOPS 158	5 <sup>h</sup> 37 <sup>m</sup> 24 <sup>s</sup> 46	-6°58′32″88	5/9.5	M/M	
HOPS 160	5 <sup>h</sup> 37 <sup>m</sup> 51 <sup>s</sup> 05	-6°47′20″40	4.7/-	$\mathbf{D}^{\prime}-$	
HOPS 166	5 <sup>h</sup> 36 <sup>m</sup> 25 <sup>s</sup> 13	-6°44′41″64	5.5/11.5	M/D	40
HOPS 168	5 <sup>h</sup> 36 <sup>m</sup> 18 <sup>s</sup> 94	-6°45′22″68	4.9/12.1	D/D	41
HOPS 169	5 <sup>h</sup> 36 <sup>m</sup> 36 <sup>s</sup> 12	-6°38′51″72	4.7/10	$\mathbf{D}'\mathbf{D}$	39
HOPS 174	5 <sup>h</sup> 36 <sup>m</sup> 25 <sup>s</sup> 85	-6°24′58″68	4/-	$\mathbf{M}^{'}\!/-$	36
HOPS 177	5 <sup>h</sup> 35 <sup>m</sup> 50 <sup>s</sup> 02	-6°34′53″40	-/10.3	-/D	37
HOPS 178	5 <sup>h</sup> 36 <sup>m</sup> 24 <sup>s</sup> 60	$-6^{\circ}22'41''16$	4.3/-	$\mathbf{D}^{\prime}-$	34
HOPS 179	5 <sup>h</sup> 36 <sup>m</sup> 21 <sup>s</sup> 84	-6°23′29″76	4.5/11.9	D/M	35
HOPS 181	5 <sup>h</sup> 36 <sup>m</sup> 19 <sup>s</sup> 51	-6°22′12″36	4/12	D/D	32
HOPS 182	5 <sup>h</sup> 36 <sup>m</sup> 18 <sup>s</sup> 84	-6°22′10″20	4/11.7	D/D	31
HOPS 192	5 <sup>h</sup> 36 <sup>m</sup> 32 <sup>s</sup> 45	$-6^{\circ}01'16''32$	7.5/10	M/M	
HOPS 198	5 <sup>h</sup> 35 <sup>m</sup> 22 <sup>s</sup> 18	$-6^{\circ}13'06''24$	-/10	-/M	
HOPS 203	5 <sup>h</sup> 36 <sup>m</sup> 22 <sup>s</sup> 85	-6°46′06″24	-/11.7	-/D	42
HOPS 355	5 <sup>h</sup> 37 <sup>m</sup> 17 <sup>s</sup> 09	$-6^{\circ}49'49''44$	4.3/10.5	M/M	.2
HOPS 368	5 <sup>h</sup> 35 <sup>m</sup> 24 <sup>s</sup> .72	-5°10′30″36	7/14	D/D	14
HOPS 370	5 <sup>h</sup> 35 <sup>m</sup> 27 <sup>s</sup> . 62	$-5^{\circ}09'33''48$	5/17	M/M	13
HOPS 383	5 <sup>h</sup> 35 <sup>m</sup> 29 <sup>s</sup> .81	$-4^{\circ}59'51''00$	9.6/-	D/-	2

#### Notes.

Aside from the lack of good source catalogs in this region, the CO velocity dispersion here can be as high as  $100 \text{ km s}^{-1}$ , due to the BN/KL "explosion" (Bally et al. 2017), making it hard to define blue/red outflow lobes. Thus, as in Tanabe et al. (2019), we focus our outflow search outside of OMC 1.

In total, we identify 45 outflows with 67 individual lobes. Of these, 11 were not identified by Tanabe et al. (2019). While we

expect all outflows to be bipolar, in several cases we only see one lobe. This could be due to interactions between the outflow and the turbulent environment or obscuration of one of the lobes by intervening dense gas (Offner et al. 2011). Alternatively, the outflow source may be close to the cloud surface, so that only one side of the outflow entrains molecular gas (e.g., Chernin & Masson 1995) or the other outflow lobe

<sup>&</sup>lt;sup>a</sup> HOPS sources are protostars in the catalog from Furlan et al. (2016). SMZ sources are sources of H<sub>2</sub> outflows in Davis et al. (2009) that are not in the HOPS catalog. <sup>b</sup> These are the visually determined velocities closest to the mean cloud velocity that most clearly separate the outflow lobes from the surrounding cloud. Entries marked with "–" indicate that one of the outflow lobes is not detected. See Section 3 for details.

<sup>&</sup>lt;sup>c</sup> Each entry has two values, referring to the blue/red lobes separately. Entries marked "D" for Definite are clearly outflows. Entries marked "M" for Marginal are unclear. See Section 3 for details.

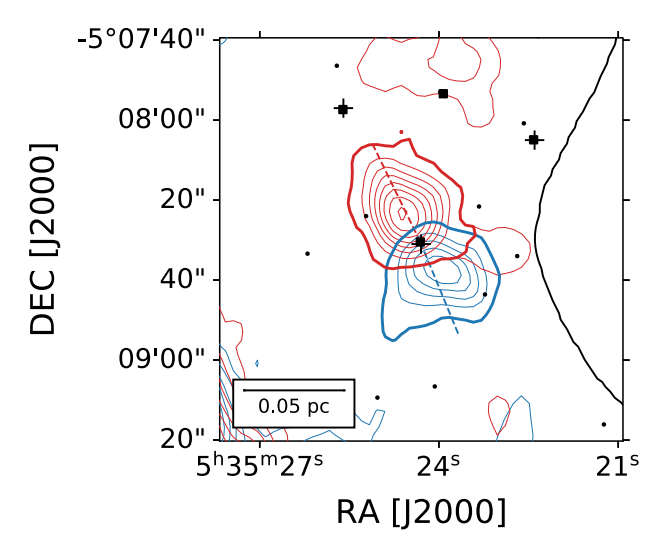


**Figure 2.** Outflow around HOPS 68. Blue (red) contours show  $^{12}$ CO integrated from  $-2 \text{ km s}^{-1}$  to  $\nu_{\text{blue}}$  ( $\nu_{\text{red}}$  to 20 km s $^{-1}$ ), where  $\nu_{\text{blue}}$  and  $\nu_{\text{red}}$  are given in Table 1. Contour levels go from 5 to 50 $\sigma$ , in steps of 5 $\sigma$  where  $\sigma$  is the rms error in the integrated map. Thick contours show the region we extract for each lobe. Black solid line shows the closest C<sup>18</sup>O filament from Suri et al. (2019). Black squares indicate HOPS protostars from Furlan et al. (2016), black crosses indicate H<sub>2</sub> outflow sources from Davis et al. (2009), and small black points indicate all Spitzer YSOs from Megeath et al. (2012).

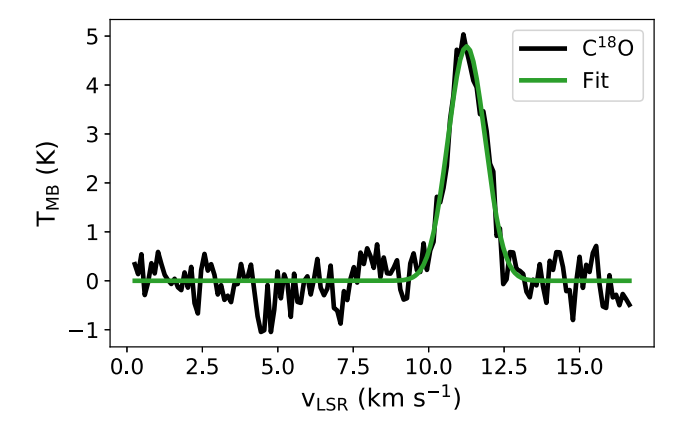


**Figure 3.** C<sup>18</sup>O spectrum toward HOPS 68. Black line shows the average C<sup>18</sup>O spectrum within a radius of 15" around HOPS 68. Green line is a Gaussian fit to the spectrum. We define the mean of this fit to be the systemic velocity  $v_{\rm sys}$  (see Section 4.1.2).

may be impossible to separate from other nearby emission (Arce & Goodman 2001a). We do not detect 10 of the outflows included in Tanabe et al. (2019). Most of these nondetections consist of the most dubious outflows in that study, which we suspect are spurious due to the automated identification method they use. Of the 67 outflow lobes, we classify 38 as "definite" and 29 as "marginal." Table 1 lists the source, location,  $v_{\rm blue}$  and  $v_{\rm red}$ , confidence score, and the corresponding outflow in Tanabe et al. (2019) for our entire catalog. Figure 1 shows the outflow catalog on a map of the peak  $^{12}{\rm CO}$  temperature.

Figure 2 shows an outflow in OMC 2 driven by HOPS 68. This outflow is well-known in the literature, listed as Outflow 12 in Tanabe et al. (2019) and FIR 2 in Takahashi et al. (2008). We use this outflow in Figures 3–9 to demonstrate our methods for calculating outflow properties. We present the entire outflow catalog in Appendix B.

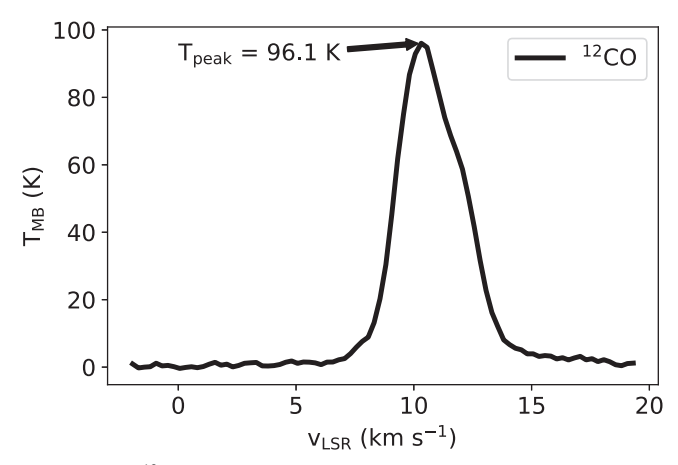


**Figure 4.** The  $^{12}$ CO spectrum of the HOPS 68 outflow. Black line shows the average  $^{12}$ CO spectrum within the outflow mask including both lobes shown in Figure 2. We use the peak of this spectrum,  $T_{\text{peak}}$ , to calculate  $T_{\text{ex}}$  (see Section 4.1.3).

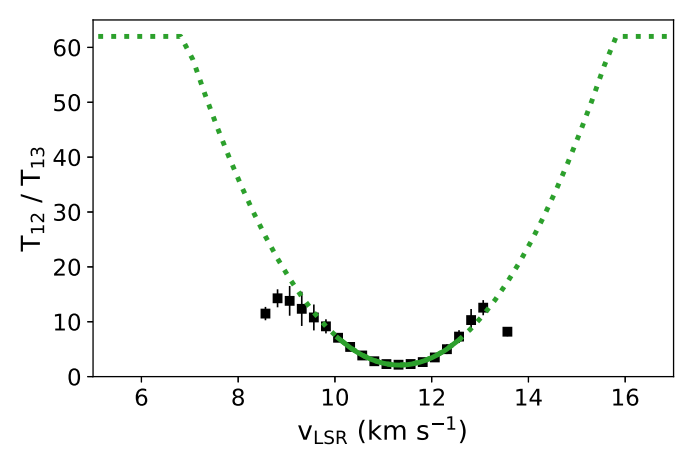


**Figure 5.** The  $^{12}\text{CO}/^{13}\text{CO}$  ratio of the HOPS 68 outflow. Black points show the average ratio between  $^{12}\text{CO}$  and  $^{13}\text{CO}$  in each velocity channel using only pixels where both lines are detected at or above  $5\sigma$ . Error bars indicate the standard deviation of the ratio. Green parabola is the weighted least-squares fit to the ratio. Solid line shows the fitting range used, while the dotted line is an extrapolation of this fit. Parabola is capped at the assumed isotopic ratio of 62 (see Section 4.1.4). Note the uncertainty on the ratio at the most extreme velocities is likely underestimated because the only pixels at these velocities lie in a small region with a size similar to the beam. Thus, the standard deviation in these pixels is lower due to the correlation between pixels.

# 4. Physical Properties of Outflows

#### 4.1. Calculating Physical Properties

To calculate the physical properties of outflows, we adapt the methods described by Arce & Goodman (2001b), Dunham et al. (2014), and Zhang et al. (2016).

#### 4.1.1. Extracting Outflow Emission

To measure the outflow mass, we must first extract each outflow from the surrounding cloud. This is particularly difficult in Orion, where many outflows are clustered and overlapping. We use a two-step approach to extract each outflow lobe.

First, we integrate the  $^{12}\text{CO}$  cube over the visually estimated velocity range of the outflow lobe (discussed in Section 3). We integrate from  $v_{\text{blue}}$  ( $v_{\text{red}}$ ) given in Table 1 to the velocity

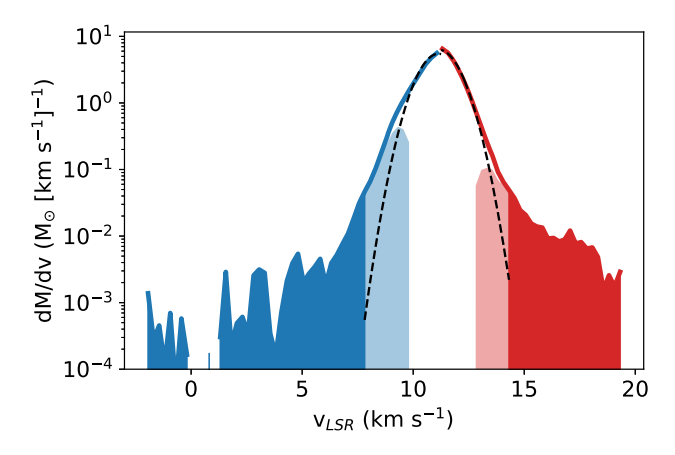


**Figure 6.** Mass spectrum of the HOPS 68 outflow. Blue (red) lines show the opacity-corrected mass spectrum in the blue (red) lobe region. Black dashed lines are Gaussian fits to these mass spectra. Dark blue (dark red) shaded regions indicate the region integrated to get the high-velocity mass, which is reported as the lower limit in Table 2. Light blue (light red) shaded regions show the low-velocity mass after subtracting the cloud mass spectrum fit (see Section 4.1.5).

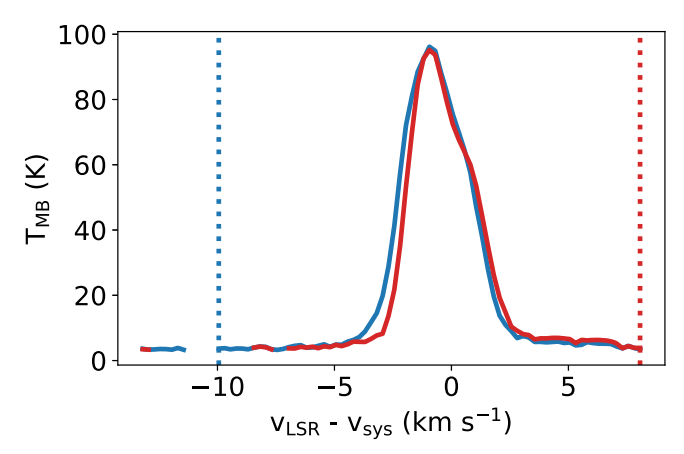


**Figure 7.** Maximum velocity of the HOPS 68 outflow. Blue (red) lines show the mean  $^{12}$ CO spectrum in the blue (red) lobe regions. Blue (red) dotted line marks the maximum blue (red) outflow velocity, defined as the first channel where  $^{12}$ CO is not detected at  $3\sigma$  (see Section 4.1.8).

extremum of the cube,  $-2 \text{ km s}^{-1}$  ( $20 \text{ km s}^{-1}$ ). We select pixels above  $5\sigma$  in this integrated map of high-velocity emission. Next, we draw a region around each outflow lobe by hand to remove other overlapping outflows or other cloud structures in the area.

To summarize, those pixels that are above  $5\sigma$  in integrated high-velocity  $^{12}\text{CO}$  and are visually inside the outflow are included in determining the physical properties of the outflow. Figure 2 shows the regions extracted for the HOPS 68 outflow. The regions extracted for the other outflows are shown in Appendix B.

#### 4.1.2. Systemic Velocity

To calculate outflow energetics, we need to know the systemic velocity  $v_{\rm sys}$  of the outflow source. We use the CARMA–NRO Orion C<sup>18</sup>O data (Kong et al. 2018) for this purpose. We fit a Gaussian model to the average C<sup>18</sup>O spectrum within a 15" radius around the outflow source and define the mean of this Gaussian to be  $v_{\rm sys}$ . In most cases, there is only one significant velocity component in the C<sup>18</sup>O spectrum. In the few outflows where multiple velocity

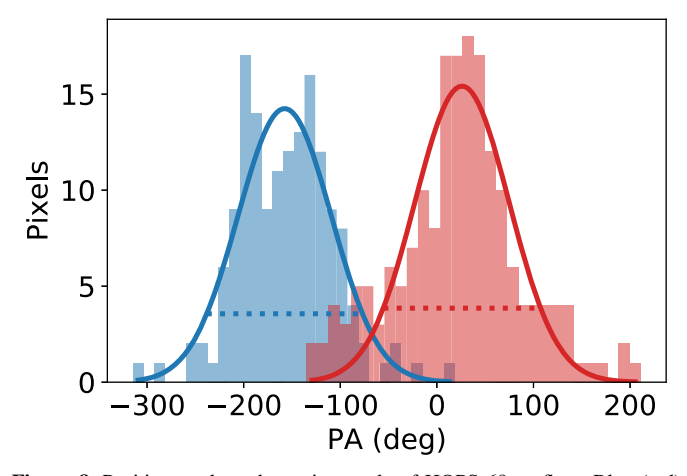


**Figure 8.** Position angle and opening angle of HOPS 68 outflow. Blue (red) histograms show the position angle distribution of all pixels in the blue (red) lobe region. Curves are Gaussian fits to these distributions. We adopt the mean of each lobe as the position angle and the full width at quarter maximum (dotted lines) as the opening angle (see Section 4.1.9).

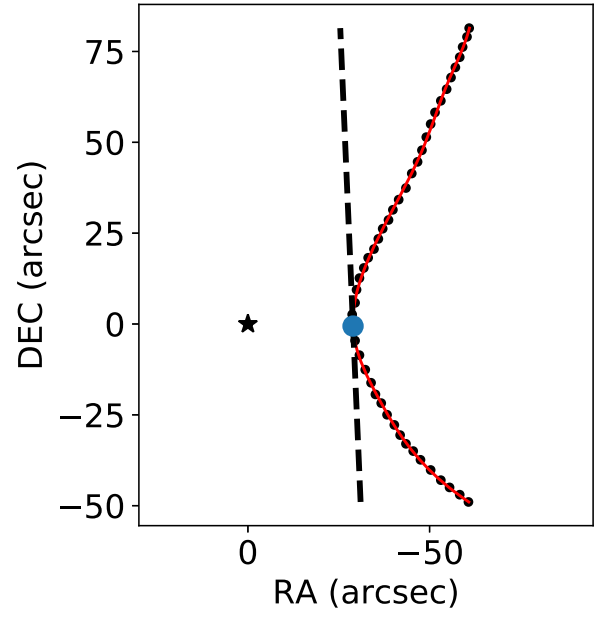


**Figure 9.** C<sup>18</sup>O filament near HOPS 68. Black points show the filament from the Suri et al. (2019) catalog closest to HOPS 68. Red curve is a smooth cubic spline interpolation of the filament. Outflow source (HOPS 68) is marked with a black star. Blue circle shows the closest point on the filament to the source. To derive the filament position angle, we find the tangent at this nearest point, shown as a black dashed line (see Section 5).

components are detected, we use the velocity of the component with the highest peak intensity. Figure 3 shows the C<sup>18</sup>O spectrum and fit for the HOPS 68 outflow.

# 4.1.3. Excitation Temperature

We estimate the excitation temperature of  $^{12}$ CO,  $T_{ex}$ , using the equation from Rohlfs & Wilson (1996), which assumes  $^{12}$ CO is optically thick in the line center:

$$T_{\rm ex} = \frac{5.53}{\ln(1 + [5.53/(T_{\rm peak} + 0.82)])}.$$
 (1)

We define  $T_{\rm peak}$  for each outflow to be the peak temperature of the average  $^{12}{\rm CO}$  spectrum within the outflow area defined

in Section 4.1.1, including both lobes if present. Figure 4 shows the average  $^{12}\text{CO}$  spectrum with  $T_{\text{peak}}$  indicated for the HOPS 68 outflow. The average  $T_{\text{ex}}$  of the outflow sample is 64 K.

While the peak  $^{12}$ CO temperature traces the bulk of the gas in the region of the outflow source, the actual outflowing gas likely has a different excitation temperature. Yang et al. (2018) find an average temperature of around 100 K for the entrained outflow gas traced by the low-J CO transitions. Above about 20 K, the mass dependence on  $T_{\rm ex}$  is close to linear. To convert a mass from one excitation temperature to another, the following formula may be used, obtained by a linear least-squares fit to the mass– $T_{\rm ex}$  relation above 20 K:

$$\frac{M_{\text{new}}}{M_{\text{old}}} = \frac{0.128 + 0.0175 \, T_{\text{ex,new}}}{0.128 + 0.0175 \, T_{\text{ex,old}}}.$$
 (2)

If the outflows in our sample have a constant  $T_{\rm ex}$  of 100 K, the outflow mass (and all properties derived from mass) will increase by an average factor of 1.5.

In Orion A, <sup>12</sup>CO is usually optically thick (Kong et al. 2018). Therefore, if we do not correct for opacity, we may miss a substantial amount of outflow mass. By comparing to more optically thin tracers, studies have long shown that outflows tend to be optically thick in <sup>12</sup>CO, at least close to cloud velocities (e.g., Goldsmith et al. 1984; Arce & Goodman 2001b). Dunham et al. (2014) find that correcting for the optical depth of outflows increases their mass by a factor of 3 on average. Despite this, outflow studies that lack an optically thin tracer often assume that all <sup>12</sup>CO outflow emission is optically thin, e.g., in Orion (Morgan et al. 1991; Takahashi et al. 2008).

Tanabe et al. (2019) adopt an average <sup>12</sup>CO optical depth of 5 for their entire outflow catalog. They apply this constant correction factor to every velocity channel. However, Dunham et al. (2014) show that the optical depth varies with velocity: optical depth decreases away from the mean cloud velocity. We follow Dunham et al. (2014) and Zhang et al. (2016) and use the ratio of <sup>12</sup>CO/<sup>13</sup>CO to derive a velocity-dependent opacity correction for each outflow.

We assume that both <sup>12</sup>CO and <sup>13</sup>CO are in LTE with the same excitation temperature and that <sup>13</sup>CO is optically thin, a reasonable assumption given the results reported in Kong et al. (2018). The ratio between the two isotopes is then

$$\frac{T_{{}^{12}\text{Co}}}{T_{{}^{13}\text{CO}}} = \frac{[{}^{12}\text{CO}]}{[{}^{13}\text{CO}]} \frac{1 - e^{-\tau_{12}}}{\tau_{12}},\tag{3}$$

where we assume the abundance ratio [ $^{12}$ CO]/[ $^{13}$ CO] is 62 (Langer & Penzias 1993) and  $\tau_{12}$  is the optical depth of  $^{12}$ CO. In each velocity channel, we calculate the average ratio between  $^{12}$ CO and  $^{13}$ CO in pixels in the outflow region with both lines detected at  $5\sigma$  or higher.

Usually, <sup>13</sup>CO is too weak to be detected more than 2–3 km s<sup>-1</sup> away from the line core. Thus, we extrapolate the measured ratio spectrum by fitting it with a second-order polynomial, weighting each velocity channel by the standard deviation of the ratio in that channel. For most of the outflows, we use a fitting range of 1.5 km s<sup>-1</sup> on either side of the minimum ratio. This fitting range is adjusted for the few outflows with multiple velocity components to ensure that the

component corresponding to  $v_{\rm sys}$  is fit. For each velocity, we use the value of this fit and Equation (3) to calculate the correction factor  $\tau_{12}/(1-e^{-\tau_{12}})$  with which we multiply the observed <sup>12</sup>CO. Because the opacity correction factor cannot be less than unity for any value of  $\tau_{12}$ , the ratio spectrum fit is capped at the value of  $\tau_{12}$  (13CO); in this regime, we consider <sup>12</sup>CO to be optically thin. In Figure 5, we show an example of the  $\tau_{12}$ CO ratio spectrum and fit for the HOPS 68 outflow.

#### 4.1.5. Outflow Mass

After correcting for opacity, we use the  $^{12}$ CO emission to calculate the  $H_2$  column density in each velocity channel. From Equation (A6) in Zhang et al. (2016),

$$\frac{dN}{dv} = \left(\frac{8\pi k \nu_{ul}^2}{hc^3 A_{ul} g_u}\right) Q_{\text{rot}}(T_{\text{ex}}) e^{E_u/kT_{\text{ex}}} \frac{T_R(v)}{f},\tag{4}$$

where  $\nu_{ul} = 115.271 \, \text{GHz}$  is the frequency of the  $^{12}\text{CO}(1-0)$  transition,  $A_{ul} = 7.203 \times 10^{-8} \, \text{s}^{-1}$  is the Einstein A coefficient,  $E_u/k = 5.53 \, \text{K}$  is the energy of the upper level,  $g_u = 3$  is the degeneracy of the upper level,  $Q_{\text{rot}}$  is the partition function (calculated to J = 100),  $T_{\text{ex}}$  is the excitation temperature defined in Section 4.1.3,  $T_R(\nu)$  is the opacity-corrected brightness temperature of  $^{12}\text{CO}$ , and f is the abundance ratio of  $^{12}\text{CO}/H_2$ . We assume an abundance ratio of  $f = 1 \times 10^{-4}$  (Frerking et al. 1982).

We then calculate the mass in each voxel:

$$M = \mu_{\rm H_2} m_{\rm H} A_{\rm pixel} N_{\rm H_2}, \tag{5}$$

where  $\mu_{\rm H_2}=2.8$  is the mean molecular weight of  $\rm H_2$  (Kauffmann et al. 2008),  $m_{\rm H}=1.674\times 10^{-24}\,\rm g$  is the mass of the hydrogen atom, and  $A_{\rm pixel}=1.6\times 10^{-5}\,\rm pc^2$  is the spatial area subtended by each pixel at the distance of the cloud. In blue (red) outflow lobes, we sum the total mass in each velocity channel blueward (redward) of  $v_{\rm sys}$  and arrive at the outflow mass spectrum dM/dv. We only consider pixels above  $3\sigma$  in a given channel and within their respective outflow lobe region in this mass calculation. Figure 6 shows an example mass spectrum for the HOPS 68 outflow.

The total mass of each outflow lobe is obtained by integrating the mass spectrum over the relevant velocity range. For a lower limit on the mass, we consider only the high-velocity component: all velocity channels farther from  $v_{\rm sys}$  than the minimum visually determined outflow velocity ( $v_{\rm blue}/v_{\rm red}$ ). These velocities were chosen to include as much outflow emission as possible while avoiding contamination by the main cloud. However, if we only consider this high-velocity outflow material, we may miss a significant fraction of the total mass.

# 4.1.6. Low-velocity Outflow Emission

Outflows are conspicuous because of their high-velocity emission, but outflows also exist at lower velocities. Dunham et al. (2014) note that escape velocities from protostars can be as low as 0.1 km s<sup>-1</sup>. As these velocities are much lower than typical cloud CO line widths, this low-velocity outflow material is often difficult to disentangle from the CO emission arising from the turbulent host molecular cloud.

The low-velocity contribution to the total outflow mass can be quite significant. Dunham et al. (2014) found that adding the

**Table 2**Outflow Physical Properties

						w Physical Pi	орегиез			
Source	Lobe	$M^{\rm a}$ $(M_{\odot})$	$P (M_{\odot} \text{ km s}^{-1})$	$E (10^{43} \text{ erg})$	R <sub>max</sub> (pc)	$v_{\text{max}}$ (km s <sup>-1</sup> )	$t_{\rm dyn} \over (10^4 {\rm yr})$	$(10^{-6} \frac{\dot{M}}{M_{\odot}} \text{ yr}^{-1})$	$(10^{-6} M_{\odot} \text{ km s}^{-1} \text{ yr}^{-1})$	$(10^{30} \text{ erg s}^{-1})$
SMZ 11	В	0.09-1.52	0.44-3.67	2.1-9.9	0.11	7.1	1.5	6.3-102.3	29.8-247.2	45.4–211.6
SMZ 17	В	0.00 – 0.16	0.01 - 0.48	0.1-1.8	0.03	9.0	0.3	0.2-48.5	2.1-145.1	6.0-172.2
•••	R	0.01 - 0.22	0.05 - 0.67	0.4 - 2.4	0.05	8.3	0.6	1.1–39.5	8.5–117.7	20.1-136.0
SMZ 21	R	0.10-1.25	0.33-2.46	1.1–5.3	0.28	5.1	5.4	1.8–23.3	6.2–46.0	6.8–31.6
SMZ 30	В	0.61-0.93	1.07–1.46	1.9–2.4	0.16	2.6	5.9	10.3–15.7	18.2–24.7	10.2–12.8
SMZ 50	В	0.08-0.21	0.22-0.47	0.6–1.1	0.22	4.8	4.4	1.8–4.8	4.9–10.6	4.4–7.9
HOPS 10	R	0.07-1.46	0.41–4.58	2.5–15.5	0.26	11.2	2.3	3.2–64.6	18.4–201.9	35.2–216.8
HOPS 11	В	0.12-0.17	0.50-0.59	2.1–2.3	0.14	9.7	1.4	9.1–12.8	36.3–43.3	48.3–52.9
	R	0.06–1.14	0.39–3.57	2.8–12.6	0.18	11.6	1.5	3.7–75.9	25.8–236.6	58.8–264.6
HOPS 12	В	1.97–2.92	8.19–9.54	35.1–37.4	0.65	10.0	6.3	31.1–46.0	129.5–150.7	174.9–186.6
HOPS 44	В	1.32–2.65	5.07-8.99	19.5–31.2	0.18	9.8	1.8	74.9–149.9	286.6–508.7	349.8–559.4
HOPS 50	В	0.13-0.13	0.22-0.22	0.5-0.5	0.28	5.4	5.1	2.5–2.5	4.4–4.4	2.8–2.8
HOPS 56 HOPS 58	R R	0.20-1.46 0.08-1.07	0.83–3.56 0.33–2.62	3.5–9.7 1.3–6.8	0.15 0.14	7.7 6.1	1.8 2.2	10.9–79.2 3.7–48.1	44.8–192.7 14.7–117.1	59.6–166.9 18.6–97.2
HOPS 59	K B	0.08-1.07	0.33-2.02	2.0-8.7	0.14	8.6	5.8	1.5–36.4	7.1–67.8	11.1–47.2
HOPS 60	В	0.09-2.12	0.41-3.93	0.3–2.1	0.31	6.7	2.0	0.7–17.0	3.3–39.3	5.1–32.1
	R	0.01-0.33	0.06-0.74	0.3-2.1	0.14	7.8	1.9	0.8–23.6	3.2–39.7	4.3–24.3
HOPS 68	В	0.01-0.44	0.15-1.17	0.2–1.4	0.15	7.8 9.9	0.5	5.9–105.4	31.0–241.9	59.7–207.5
	R	0.05-0.31	0.13-1.17	1.2–1.8	0.05	8.1	0.7	7.6–26.6	35.9–78.4	57.3–88.4
HOPS 70	R	0.12-0.37	0.42-0.99	1.5–2.8	0.10	5.6	1.7	7.0–20.9	24.1–56.6	26.5–50.9
HOPS 71	В	0.12-0.57	0.78-7.64	3.5–18.4	0.10	6.8	4.9	3.6–75.7	15.9–157.0	22.9–119.4
HOPS 75	R	0.03-0.25	0.10-0.49	0.3–1.1	0.07	4.6	1.6	1.9–15.9	6.2–31.1	6.3–21.1
HOPS 78	В	0.32–7.86	2.15–21.91	15.0–71.5	0.40	13.3	2.9	10.8–268.9	73.4–749.4	162.3–774.9
	R	0.18-3.44	0.79–7.05	3.7–16.8	0.33	8.0	4.1	4.3–84.2	19.4–172.1	28.6–130.1
HOPS 81	В	0.07-1.00	0.36–2.34	1.9–6.5	0.16	10.1	1.6	4.5–62.7	22.2–145.9	37.3–128.0
	R	0.02-0.09	0.04-0.15	0.1-0.3	0.05	3.2	1.6	1.2–5.5	2.8–9.5	2.2–5.5
HOPS 84	В	0.02-0.12	0.05-0.19	0.1-0.3	0.12	4.4	2.7	0.6–4.3	1.8–7.0	1.6–4.0
	R	0.80-2.62	2.81–7.23	9.9–20.8	0.83	8.7	9.4	8.6–27.9	29.9–76.9	33.4–70.1
HOPS 87	В	1.07-2.09	3.44-5.63	11.6-16.3	0.25	7.2	3.5	30.7-60.3	99.5-162.7	106.3-149.4
	R	0.02 - 0.27	0.06-0.45	0.2 - 0.8	0.08	4.6	1.7	1.2-15.7	3.3-25.7	3.0-14.6
HOPS 88	В	0.17 - 1.02	0.70 - 2.45	3.0-6.8	0.09	9.1	0.9	18.8-111.3	76.0-268.3	105.3-236.7
	R	0.05 - 0.10	0.15-0.26	0.5 - 0.7	0.08	6.9	1.1	4.3-9.7	13.7-24.0	14.4-20.8
HOPS 92	В	0.37 - 2.44	1.51-5.70	6.4-15.4	0.32	8.8	3.5	10.5-69.1	42.7-161.6	57.4-138.1
	R	0.12 - 0.17	0.41 - 0.47	1.4-1.5	0.48	6.2	7.6	1.6-2.3	5.4-6.2	5.8-6.1
HOPS 96	В	0.04 - 0.09	0.10 - 0.16	0.3 - 0.4	0.10	4.0	2.6	1.5-3.4	4.1-6.2	3.8-4.5
•••	R	0.32 - 1.54	0.68 - 2.43	1.4-4.0	0.23	4.7	4.7	6.9-32.9	14.6-52.1	9.8-27.1
HOPS 99	В	0.03 - 0.06	0.06-0.09	0.1-0.1	0.13	2.6	4.7	0.7-1.3	1.3-2.0	0.8 - 1.0
HOPS 157	В	0.03 - 0.03	0.07 - 0.07	0.2 - 0.2	0.10	3.4	2.9	1.0-1.0	2.5–2.5	2.0-2.0
HOPS 158	В	0.08 – 0.17	0.20 - 0.37	0.5 - 0.8	0.11	4.1	2.6	2.9-6.4	7.6–13.9	6.5–10.1
•••	R	0.02 - 0.03	0.07 - 0.08	0.2 - 0.2	0.07	3.9	1.9	1.3–1.8	3.6-4.2	3.6-3.8
HOPS 160	В	0.06-0.06	0.10-0.10	0.2 - 0.2	0.11	3.2	3.3	1.9–1.9	2.9–2.9	1.5–1.5
HOPS 166	В	0.02 - 0.47	0.09-1.03	0.3 - 2.4	0.06	5.8	1.1	2.3-43.6	8.5–95.9	10.1–70.7
	R	0.93–2.65	3.46–7.26	13.6–22.2	0.41	10.7	3.8	24.7–70.5	92.2–193.6	115.9–188.1
HOPS 168	В	0.01-0.05	0.03-0.10	0.1-0.3	0.09	6.1	1.4	0.4–3.3	2.1–7.2	3.2–6.3
	R	0.96-6.97	4.30–15.22	20.9–42.7	1.16	10.4	10.9	8.8–63.8	39.3–138.8	60.7–123.8
HOPS 169	В	0.09-0.23	0.46–0.66	2.6–2.9	0.24	8.9	2.7	3.4–8.5	17.3–24.8	30.9–34.5
	R	0.13–1.11	0.74–2.33	4.8–7.6	0.22	12.3	1.8	7.4–62.0	41.5–130.7	85.3–135.0
HOPS 174	В	0.07-0.15	0.20-0.37	0.6–1.0	0.20	4.4	4.4	1.6–3.3	4.6–8.3	4.3–6.9
HOPS 177	R	0.72-0.99	1.42–1.74	3.0–3.4	0.30	7.3	4.0	17.9–24.6	35.1–43.2	23.7–26.8
HOPS 178	В	0.18-0.52	0.58–1.33	1.9–3.6	0.21	8.9	2.3	7.9–22.6	25.4–58.1	26.3–49.6
HOPS 179	В	0.06-0.06	0.15-0.15	0.4–0.4	0.08	4.6	1.8	3.2–3.2	8.4–8.4	7.2–7.2
	R	0.04-0.84	0.22-2.92	1.4–11.1	0.12	12.4	0.9	3.9–90.6	24.2–315.8	49.5–378.0
HOPS 181	В	0.48-0.91	1.94–3.17	8.3–11.7	0.21	9.1	2.2	21.4–40.9	87.2–142.2	117.9–167.2
 HOPS 182	R B	0.25–9.97 0.29–0.52	1.46–24.75 1.25–1.87	9.1–72.0 5.7–7.4	1.14 0.21	12.1 9.1	9.2 2.3	2.7–108.0 12.8–22.7	15.8–268.4 55.1–82.5	31.2–247.6 79.3–103.6
	R	0.29-0.32	0.62-4.22	3.7–7.4	0.21	9.1 11.1	4.6	2.2–27.3	13.3–90.8	26.2–105.3
 HOPS 192	K B	0.10-1.26	0.62-4.22	1.3–1.3	0.55	4.1	2.4	30.1–30.1	38.0–38.0	26.2–105.3 17.6–17.6
HOPS 192	B R	0.72-0.72	0.05-0.13	0.1–0.2	0.10	3.7	2.4 1.7	30.1–30.1 1.4–4.6	38.0–38.0 2.9–7.5	2.1–4.2
HOPS 198	R	0.02-0.08	0.03-0.13	0.1-0.2	0.10	6.0	1.7	0.3–11.2	1.4–27.9	2.1–4.2
HOPS 203	R	0.42-0.42	0.02=0.47	2.1–2.1	0.10	5.7	3.3	12.6–12.6	27.6–27.6	20.3–20.3
HOPS 355	В	0.42-0.42	1.31–1.38	4.7–4.8	0.19	8.9	3.3 4.7	7.9–9.2	27.6–27.0	31.6–32.2
	R	0.03-0.20	0.12-0.51	0.5–1.4	0.43	7.8	6.0	0.5–3.4	2.0-8.5	2.7–7.4
HOPS 368	В	0.03-0.20	0.12-1.28	0.6–3.6	0.06	6.7	0.8	3.0-59.9	13.9–153.0	21.1–135.1
1101 5 500	ъ	0.02 0.50	0.12 1.20	0.0 5.0	0.00	0.7	0.0	3.0 37.7	15.7 155.0	21.1 133.1

Table 2 (Continued)

Source	Lobe	$M^{\mathrm{a}}$ $(M_{\odot})$	$P (M_{\odot} \text{ km s}^{-1})$	$E (10^{43} \text{ erg})$	R <sub>max</sub> (pc)	$v_{\text{max}}$ (km s <sup>-1</sup> )	$t_{\rm dyn} (10^4  \rm yr)$	$(10^{-6} \frac{\dot{M}}{M_{\odot}} \text{ yr}^{-1})$	$\dot{P}$ $(10^{-6} M_{\odot} \text{ km s}^{-1} \text{ yr}^{-1})$	$(10^{30} \text{ erg s}^{-1})$
	R	0.02-0.05	0.09-0.15	0.3-0.5	0.04	6.3	0.6	3.6-8.1	13.7–24.1	17.0–24.8
HOPS 370	В	0.05 - 0.33	0.38 - 1.31	3.3-6.7	0.13	13.1	1.0	4.6-33.2	38.2-131.9	105.3-214.5
	R	0.02 - 0.56	0.11-1.26	0.7 - 3.6	0.12	8.1	1.5	1.1-37.9	7.3-85.7	15.5-77.7
HOPS 383	В	0.27-0.34	0.69-0.82	1.9–2.1	0.15	5.4	2.8	9.9–12.4	25.0–29.7	21.3–23.9
Total <sup>b</sup>		15.4–76.9	55.6–193	232–573				499–2618	1855–6824	2551–6666

#### Notes.

inferred low-velocity emission increased the mass of outflows by a factor of 7.7 on average, with some outflows increasing by an order of magnitude or more. Outflow momentum and energy increased by factors of 3 to 5, on average. Offner et al. (2011) found that using only high-velocity outflow emission underestimated the total outflow mass by a factor of 5 in synthetic observations of simulated outflows. Clearly, low-velocity emission should be accounted for when assessing the absolute impact of outflows on the cloud. We describe our method, adapted from Dunham et al. (2014), for recovering this low-velocity outflow mass below.

For each outflow lobe, we fit the opacity-corrected mass spectrum with a Gaussian. For "low" velocities between  $v_{\rm sys}$  and the visually determined minimum outflow velocity ( $v_{\rm blue}$  or  $v_{\rm red}$ ), we subtract this Gaussian fit from the mass spectrum and define any excess mass as low-velocity outflow mass. To reduce the amount of extraneous cloud mass introduced with this method, we exclude all velocity channels within 1 km s<sup>-1</sup> of  $v_{\rm sys}$ . Figure 6 demonstrates this procedure for the HOPS 68 outflow.

Generally, the low-velocity outflow mass is significantly greater than the mass at high velocities. Because this method assumes the cloud mass spectrum is fitted well by a Gaussian, we expect that the low-velocity mass will often be contaminated by ambient cloud material. Thus, for each outflow lobe, we consider the high-velocity outflow mass to be a lower limit and the high-velocity plus low-velocity mass to be an upper limit on the total outflow lobe mass. We report these mass ranges for each outflow lobe in Table 2.

## 4.1.7. Momentum and Kinetic Energy

We define the momentum per velocity channel to be  $dP/dv = (dM/dv)v_{\rm out}$ , where dM/dv is the mass spectrum discussed in Section 4.1.5 and  $v_{\rm out}$  is the velocity relative to  $v_{\rm sys}$ . Similarly, the kinetic energy per velocity channel is  $dE/dv = (1/2)(dM/dv)v_{\rm out}^2$ . We sum the momentum and kinetic energy separately for low velocities, with the ambient cloud–corrected mass spectrum, and high velocities. In Table 2, we report the momentum and kinetic energy of each outflow lobe.

# 4.1.8. Dynamical Time

We use the same method as Curtis et al. (2010) to estimate the dynamical time  $t_{\rm dyn}$  of each outflow lobe. Assuming the outflow has been expanding uniformly at the same velocity

since it was launched,  $t_{\rm dyn} = R/v_{\rm max}$ , where R is the length of the outflow and  $v_{\rm max}$  is the maximum outflow velocity. We define R to be the projected distance from the outflow source to the farthest part of the outflow lobe, and  $v_{\rm max}$  as the minimum velocity relative to  $v_{\rm sys}$ , where  $^{12}{\rm CO}$  is not detected at  $3\sigma$ . Some outflows are detectable all the way to the limits of the  $^{12}{\rm CO}$  spectral coverage ( $-2~{\rm km~s}^{-1}$  in the blue,  $20~{\rm km~s}^{-1}$  in the red, relative to the LSR). In these cases,  $v_{\rm max}$  is a lower limit, as are the mass and mass-derived properties. Figure 7 shows our determination of  $v_{\rm max}$  for the HOPS 68 outflow. We report R,  $v_{\rm max}$ , and  $t_{\rm dyn}$ , for each outflow lobe in Table 2.

We also calculate the mass-loss rate, momentum injection rate, and energy injection rate by dividing the outflow mass, momentum, and kinetic energy by  $t_{\rm dyn}$ . In Section 4.2, we use these quantities to compare the impact of outflows to turbulence in the cloud.

#### 4.1.9. Outflow Position Angle and Opening Angles

Most studies estimate the outflow position angle (PA) by eye (e.g., Morgan et al. 1991; Takahashi et al. 2008; Plunkett et al. 2013; Stephens et al. 2017; Kong et al. 2019; Tanabe et al. 2019). We adopt a more reproducible and objective method to measure outflow position and opening angles (OA) modeled after the simulated outflow analysis carried out by Offner et al. (2011).

For each outflow lobe, we make an initial guess of the PA, measured counterclockwise (east) from the north celestial pole by convention. This initial guess is the angle from the outflow source to the peak of the integrated <sup>12</sup>CO over the velocity range of the outflow lobe. Next, we calculate the angle of every pixel in the outflow lobe relative to this initial guess. We fit the distribution of these angles with a Gaussian and define the mean of the Gaussian to be the PA of that outflow lobe. We define the OA of the outflow to be the full width at quarter maximum of the Gaussian, following the definition by Offner et al. (2011). We find this automated method does a suitable job producing a similar PA and OA to a visual determination. Furthermore, when comparing the outflow PA with filament orientation (Section 5), we avoid the risk of an artificial correlation produced by unintentional measurement bias. Figure 8 shows the distribution of pixel position angles and Gaussian fit for the HOPS 68 outflow. The PA and OA of each outflow lobe, along with their uncertainties from the Gaussian fit, are listed in Table 3.

<sup>&</sup>lt;sup>a</sup> Mass and all properties derived from mass are given as lower and upper limits. The lower limit refers to the high-velocity component of the outflow only. The upper limit refers to the sum of the high-velocity and low-velocity components. See Section 4.1.5 for details.

<sup>&</sup>lt;sup>b</sup> The total of the lower and upper limits for each column are given. The physical properties in this table are not corrected for inclination angle. See Section 4.2 for a discussion of the inclination correction.

 Table 3

 Outflow Angles and Filament Comparison

Source	Position Angle <sup>a</sup>	Opening Angle	γ <sup>b</sup> (°)	$d_{\mathrm{fil}}^{\mathrm{c}}$
	(°)	(°)	(°)	(pc)
SMZ 11	$-35 \pm 3.1/-$	$157\pm10/-$	27/-	0.064
SMZ 17	$-118 \pm 11/34 \pm 3.1$	$193 \pm 38/79 \pm 10$	10/38	0.01
SMZ 21	$-/179 \pm 0.5$	$-/35\pm2$	-/43	0.016
SMZ 30	$20\pm20/-$	$120 \pm 1.2e + 02/-$	35/-	0.11
SMZ 50	$2 \pm 1.4/-$	$77\pm8.8/-$	36/-	0.19
HOPS 10	$-/19 \pm 2$	$-/58\pm6.8$	-/71	0.003
HOPS 11	$172 \pm 1.2/16 \pm 1.7$	$92 \pm 4.1/68 \pm 5.6$	62/86	0.051
HOPS 12	$-11 \pm 0.1 / -$	$39 \pm 0.4/-$	54/-	0.031
HOPS 44	$-24\pm2.4/-$	$120 \pm 8.9/-$	70/-	0.013
HOPS 50	$-15\pm0.4/-$	$42 \pm 1.3/-$	16/-	0.005
HOPS 56	$-/119 \pm 6$	$-/191 \pm 23$	-/33	0.047
HOPS 58	$-/74\pm0.6$	$-/44 \pm 1.9$	-/88	0.056
HOPS 59	$-26\pm0.2/-$	$15 \pm 0.7 / -$	38/-	0.052
HOPS 60	$-104 \pm 0.3/57 \pm 0.3$	$22 \pm 1.1/24 \pm 0.9$	78/83	0.055
HOPS 68	$-158 \pm 3.8/26 \pm 3.7$	$161 \pm 13/163 \pm 12$	20/24	0.056
HOPS 70	$-/48 \pm 2$	$-/83\pm7.5$	-/74	0.015
HOPS 71	$39 \pm 0.6 / -$	$35 \pm 2.3/-$	59/-	0.1
HOPS 75	$-/175 \pm 1.6$	$-/95\pm5.5$	-/17	0.003
HOPS 78	$-85 \pm 0.5/80 \pm 0.2$	$41 \pm 1.5/37 \pm 0.8$	59/43	0.045
HOPS 81	$-154 \pm 0.6/34 \pm 3.1$	$51 \pm 2/83 \pm 12$	40/32	0.065
HOPS 84	$78 \pm 0.7/-93 \pm 0.2$	$38 \pm 2.4/18 \pm 0.6$	58/49	0.054
HOPS 87	$-100 \pm 0.3/118 \pm 1.2$	$49 \pm 1.2/47 \pm 4.5$	27/11	0.008
HOPS 88	$-100 \pm 3.5/82 \pm 1.7$	$210 \pm 12/99 \pm 6.1$	36/35	0.022
HOPS 92	$89 \pm 0.3 / -89 \pm 0.2$	$33 \pm 1.2/24 \pm 0.4$	43/41	0.019
HOPS 96	$69 \pm 0.8/-95 \pm 5$	$46 \pm 2.8/142 \pm 19$	55/71	0.007
HOPS 99	$-49 \pm 1.3/-$	$64\pm4.8/-$	48/-	0.003
HOPS 157	$112 \pm 1.4/-$	$66\pm4.8/-$	84/-	1.5
HOPS 158	$66 \pm 1.4/-114 \pm 2.7$	$84 \pm 4.7/113 \pm 9.1$	50/50	1.1
HOPS 160	$-38 \pm 1.1/-$	$68 \pm 3.6 / -$	2/-	0.41
HOPS 166	$99 \pm 4.9/0 \pm 1.1$	$239 \pm 17/80 \pm 3.7$	59/40	0.035
HOPS 168	$-7 \pm 3.2/160 \pm 0.2$	$101 \pm 11/33 \pm 0.6$	83/69	0.001
HOPS 169	$15 \pm 0.5/-179 \pm 0.9$	$46 \pm 1.7/62 \pm 2.9$	49/35	0.004
HOPS 174	$13 \pm 0.4 / -$	$35 \pm 1.3/-$	85/-	0.004
HOPS 177	$-/-6\pm0.7$	$-/54 \pm 2.4$	-/6	0.091
HOPS 178	$77 \pm 2/-$	$94 \pm 6.7/-$	76/-	0.04
HOPS 179	$164 \pm 1.1/16 \pm 0.8$	$60 \pm 3.6/71 \pm 2.6$	60/28	0.088
HOPS 181	$-40 \pm 2/177 \pm 0.4$	$131 \pm 7.8/24 \pm 1.2$	48/12	0.2
HOPS 182	$41 \pm 2.5/-157 \pm 0.1$	$77 \pm 8.2/9 \pm 0.3$	33/16	0.22
HOPS 192	$95 \pm 2.8/-67 \pm 1.6$	$104 \pm 9.3/105 \pm 5.3$	53/34	0.044
HOPS 198	$-/112 \pm 4.2$	$-/64 \pm 14$	-/0	0.11
HOPS 203	$-/139 \pm 4.5$	$-/60 \pm 15$	-/85	0.011
HOPS 355	$-104 \pm 0.4/98 \pm 0.1$	$45 \pm 1.3/8 \pm 0.3$	75/84	0.096
HOPS 368	$30 \pm 12/175 \pm 4.5$	$289 \pm 44/135 \pm 15$	61/84	0.032
HOPS 370	$36 \pm 1.3/24 \pm 0.5$	$66 \pm 4.8/40 \pm 1.9$	37/48	0.042
HOPS 383	$128 \pm 0.5/-$	$49 \pm 1.7/-$	88/-	0.018

#### Notes

# 4.2. Impact of Outflows on the Cloud

Protostellar outflows may be important in the maintenance of turbulence in clouds, at least at cluster scales (Nakamura & Li 2007). The efficiency of turbulent driving by outflows is highly uncertain, depending on the transfer of momentum from outflowing gas to the cloud. To be even a plausible source of turbulence with perfect outflow—cloud coupling, the aggregate

impact of outflows must be of a magnitude similar to that of the observed turbulent dissipation.

The total outflow momentum, kinetic energy, and their injection rates are given in the last row of Table 2. We report lower and upper limits on these aggregate values by summing each outflow's high-velocity component and high-velocity + low-velocity components, respectively (see Section 4.1.6).

<sup>&</sup>lt;sup>a</sup> Columns with two entries refer to the blue/red outflow lobes separately. Entries marked "-" refer to lobes that are not detected.

 $<sup>^{\</sup>rm b}$   $\gamma$  is the projected angle between the outflow and filament. See Section 5 for details.

 $<sup>^{\</sup>rm c}$   $d_{\rm fil}$  is the minimum distance between the outflow source and filament.

Te compare the aggregate outflow impact with the momentum and kinetic energy dissipation rates of the turbulent cloud, we follow the methods described in Sections 5.1.2 and 5.1.3 of Feddersen et al. (2018). Because we avoid the OMC 1 region in our outflow search, we remove the region with decl. between  $-5^{\circ}31'44''$  and  $-5^{\circ}15'33''$ , which corresponds to the gap in the HOPS protostar catalog. We select pixels where  $^{13}$ CO is detected at  $3\sigma$  to calculate the total molecular mass, velocity dispersion, and kinetic energy. To calculate the dissipation time (Equation (5) in Feddersen et al. 2018), we assume a cloud diameter of 12 pc (the geometric mean of the cloud's projected width and length) and calculate a mean onedimensional velocity dispersion of 1.7 km s<sup>-1</sup>. To calculate the momentum dissipation rate (Equation (6) in Feddersen et al. 2018), we assume a cloud radius of 6 pc and use the calculated total mass and median velocity dispersion. Excluding the OMC 1 region, we find a total momentum dissipation rate of  $\dot{P}_{turb} = 1.3 \times 10^{-2} M_{\odot} \text{ km s}^{-1} \text{ yr}^{-1}$  and a total kinetic energy dissipation rate of  $\dot{E}_{\text{turb}} = 1.4 \times 10^{34} \, \text{erg s}^{-1}$ . We compare these turbulent dissipation rates to the

We compare these turbulent dissipation rates to the aggregate outflow injection rates in Table 2,  $\dot{P}$  and  $\dot{E}$ . If we only account for the high-velocity outflow components,  $\dot{P}$  is 14% of  $\dot{P}_{turb}$  and  $\dot{E}$  is 18% of  $\dot{E}_{turb}$ . If we add the low-velocity outflow emission,  $\dot{P}$  is 51% of  $\dot{P}_{turb}$  and  $\dot{E}$  is 47% of  $\dot{E}_{turb}$ .

The outflow physical properties tabulated in Table 2 are not corrected for the inclination of outflows to the line of sight. Essentially, this means we assume that the radial velocity of outflow emission with respect to the source velocity is equivalent to the actual velocity of the outflowing gas. The closer an outflow is to the plane of the sky, the larger the discrepancy between observed and actual velocities. The outflow length  $R_{\rm max}$ , which we use to calculate  $t_{\rm dyn}$  and all the derived injection rates, should also be corrected for the outflow inclination.

Because we do not know the actual inclination of each outflow, we estimate the effect of inclination on the aggregate outflow impact by assuming the same average inclination for every outflow. The average inclination angle, assuming any orientation is equally likely, is 57°.3 (where 0° is a pole-on outflow).

Dunham et al. (2014) summarize the inclination dependence of each outflow property in their Table 8. If all of the outflows are inclined 57°.3, the total  $\dot{P}$  ( $\dot{E}$ ) will increase by a factor of 2.9 (5.3). Thus, after correcting for average inclination,  $\dot{P}$  is 41%–148% of  $\dot{P}_{turb}$  and  $\dot{E}$  is 96%–252% of  $\dot{E}_{turb}$  (depending on whether low-velocity emission is included).

We note that this inclination correction assumes that all outflow motions are along the axis of the flow, with no transverse motions. Dunham et al. (2014) caution that the inclination correction factors may be significantly smaller if transverse motions are present, as demonstrated by simulations from Downes & Cabrit (2007). The same simulations show that accounting for *atomic* gas results in additional momentum and energy of about the same magnitude as the inclination corrections discussed above. While the absolute impact of outflows in Orion A remains highly uncertain, it is safe to say a significant fraction of the turbulent dissipation could be offset if outflows couple efficiently to the cloud.

# 5. Outflow-filament Alignment

Outflows are ejected along the angular momentum axis of the protostar. If mass accretion proceeds hierarchically, from larger scales of the cloud down to the protostellar scale, then the angular momentum axis of the protostar will trace the orientation of mass accretion flows (Bodenheimer 1995). Protostars tend to form along narrow filaments of dense gas (Arzoumanian et al. 2011), and may accrete mass either along (parallel to) or across (perpendicular to) their host filaments, as seen for example in the simulations of Li et al. (2018). If one of these modes dominates protostellar mass accretion in filaments, we may expect to see a preferential direction of the angular momentum (and thus the outflow) with respect to the filament axis.

In simulations, Offner et al. (2016) find that binaries formed via turbulent fragmentation of protostellar cores produce outflows with variable position angles, and they predict a random distribution of outflow orientations under this turbulent fragmentation model. Li et al. (2018) find outflows form preferentially perpendicular to filaments in their simulations of a strongly magnetized cloud.

The alignment between CO outflows and filaments has been studied in the Perseus molecular cloud by Stephens et al. (2017) and in a massive infrared dark cloud (IRDC) by Kong et al. (2019). In Perseus, Stephens et al. (2017) showed that a sample of 57 outflows are consistent with being randomly oriented with respect to the filament, neither parallel nor perpendicular. In the IRDC G28.37+0.07, Kong et al. (2019) identified 64 outflows and showed that they are preferentially perpendicular to the filament axis. It remains to be seen whether this discrepancy arises from some meaningful difference between these clouds (e.g., evolutionary state or magnetic field strength) or by chance.

In Orion, Davis et al. (2009) showed that  $H_2$  outflows appear randomly oriented on the sky, showing no preferential alignment to the north–south integral-shaped filament. Tanabe et al. (2019) studied the outflows in single-dish CO maps, finding no evidence for alignment between outflows and the large-scale filamentary structure in the cloud. However, the filamentary structure in Orion A is more complex than a single north–south integral-shaped filament. Therefore, we use the  $C^{18}O$  filaments identified by Suri et al. (2019) in our analysis.

# 5.1. C<sup>18</sup>O Filaments

Suri et al. (2019) apply the Discrete Persistent Structures Extractor (DisPerSE; Sousbie 2011) to extract filaments from the C<sup>18</sup>O spectral cube. DisPerSE connects local maxima and saddle points in the intensity distribution, which are defined as filaments. Suri et al. (2019) identify a total of 625 filaments across the Orion A cloud, each of which are defined by their PPV coordinates, allowing filaments that overlap spatially to be separated in velocity space.

For each outflow source, we search for the closest filament. Because most of the outflow sources are located along lines of sight with a single significant C<sup>18</sup>O velocity component, we ignore the filament velocity information and only consider projected distance on the sky. We use cubic spline interpolation to approximate the discrete filament coordinates with a smooth curve. For this spline interpolation, we used the splrep and splev functions from the scipy interpolate package.

We take the slope of the tangent to the filament curve at the closest point to the outflow source to be the position angle of the filament, which is constrained to be between  $-180^{\circ}$  and  $180^{\circ}$ . Figure 9 shows an example of the spline interpolation

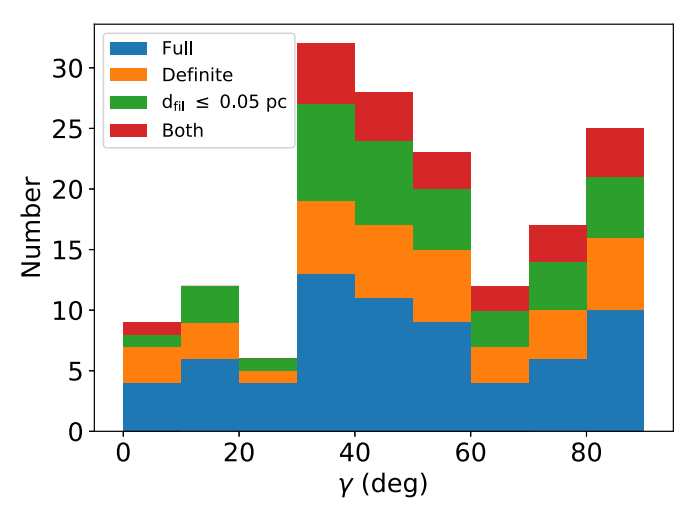


Figure 10. Distribution of projected angle between outflows and filaments. Blue histogram shows the distribution of  $\gamma$  in 10° bins for the full sample of 67 outflow lobes. Orange bars show the distribution of  $\gamma$  for the subsample of 38 outflow lobes with a confidence grade of "Definite" (Table 1). Green bars show the subsample of 37 outflow lobes whose sources are within 0.05 pc of the nearest filament (Table 3). Red bars show the subsample of 22 outflow lobes that satisfy both of these conditions. Note that the total height of the stacked bars does not equal the size of the full sample, since the subsamples are already contained within the full sample shown in blue.

and tangent fitting for the closest filament to the HOPS 68 outflow.

#### 5.2. Projected Angle between Outflows and Filaments

We follow Stephens et al. (2017) and Kong et al. (2019) in our definition of the angular separation between outflow and filament position angles,  $\gamma$ . For each outflow lobe, we define  $\gamma$  to be

$$\gamma = MIN\{|PA_{out} - PA_{fil}|, 180^{\circ} - |PA_{out} - PA_{fil}|\}, \quad (6)$$

where  $PA_{out}$  and  $PA_{fil}$  are the position angles of the outflow lobe and the closest filament, respectively. The value of  $\gamma$  for each outflow lobe is given in Table 3. Figure 10 shows the distribution of  $\gamma$ . The full sample of  $\gamma$  shows no obvious clustering at either 0 or 90°.

Many of the outflows in our catalog are not as clear as our example outflow driven by HOPS 68. Outflows categorized as "Marginal" in Table 1 are likely to have less reliable position angles. In these cases, we either have difficulty disentangling the high-velocity emission near these sources and/or we are unsure of which protostar is driving the outflow. Both of these factors could greatly affect the measured position angle, and by extension,  $\gamma$ . Stephens et al. (2017) argue that the incorrect assignment of driving sources led Anathpindika & Whitworth (2008) to erroneously conclude that outflows and filaments are perpendicular in the Perseus molecular cloud.

To test whether more reliable outflows have a different distribution of  $\gamma$ , we consider a subsample of outflow lobes which we consider "Definite" (Table 1). Figure 10 shows that these outflows are not distributed significantly differently from the full sample.

Aside from the uncertainties in calculating the outflow position angles discussed above, we consider the difficulty of assigning even a well-known outflow to a particular filament. Even though we select for the closest filament to each outflow source, we cannot exclude the possibility that other nearby

filaments may be important to the environment of an outflow. In particular, the OMC-4 region contains spatially overlapping filaments that are distinct in velocity space (Suri et al. 2019), similar to the fibers identified by Hacar et al. (2013). The incorrect assignment of outflows to filaments may introduce noise to the distribution of  $\gamma$  and mask an underlying correlation between outflow and filament orientations. To address this concern, we compare the full sample to the closest outflow-filament pairs. We adopt a threshold on the projected outflow-filament distance ( $d_{\rm fil}$ ) based on the typical filament width

Suri et al. (2019) found an average filament FWHM of approximately 0.1 pc, similar to the "characteristic" filament width found using Herschel dust continuum maps (e.g., Arzoumanian et al. 2011; Koch & Rosolowsky 2015) However, Suri et al. (2019) find a much larger spread in filament widths (about an order of magnitude around the mean). This is likely due to the fact that they allow the filament width to vary along its length, while most studies average the width over the entire filament. Motivated by the mean filament width, we choose a threshold of  $d_{\rm fil} \leq 0.05$  pc, which corresponds to an outflow source within the FWHM of an average filament. Figure 10 shows the distribution of  $\gamma$  for this subset of outflows.

Figure 10 shows that limiting the sample to the closest outflow-filament pairs with the highest confidence reduces the fraction of outflows at projected angles of  $0^{\circ}$ – $30^{\circ}$  with respect to their filaments. We stress that these angles are projected on the plane of the sky. To determine whether these outflows are preferentially aligned with the filaments, we must consider the underlying distribution of deprojected  $\gamma$ : the outflow-filament alignment in 3D.

# 5.3. The 3D Outflow-filament Alignment

An outflow-filament pair can appear at various relative orientations on the plane of the sky, depending on the line of sight. For example, an outflow observed parallel to a nearby filament may actually be perpendicular in space. Thus, we follow Stephens et al. (2017) and Kong et al. (2019) and run Monte Carlo simulations<sup>8</sup> of random vector pairs to project different underlying distributions of  $\gamma_{3D}$  onto the plane of the sky

We first generate  $10^7$  pairs of unit vectors uniformly distributed around the unit sphere. From this random uniform distribution, we make two subsets. In the "parallel" subset, we keep only those vector pairs separated by  $0^\circ-20^\circ$ . In the "perpendicular" subset, we keep the pairs separated by  $70^\circ-90^\circ$ . We also consider the full random uniform distribution of vector pairs, dubbed "random." Next, we project these vectors onto the plane of the sky by setting one coordinate to zero and calculate the projected angle between them,  $\gamma$ . By comparing the distribution of observed  $\gamma$  with the distribution of  $\gamma$  in the simulated random, parallel, and perpendicular sets of vector pairs, we investigate which of these underlying scenarios is most likely given the observations.

Figure 11 shows the cumulative distribution of  $\gamma$  for the Monte Carlo simulations and each of the outflow-filament samples discussed in Section 5.2. Compared to the random distribution of  $\gamma$ , the outflow samples have a deficit at  $\gamma < 40^{\circ}$ .

 $<sup>^{8}</sup>$  See Appendix A of Stephens et al. (2017) for a detailed description of the Monte Carlo simulations.

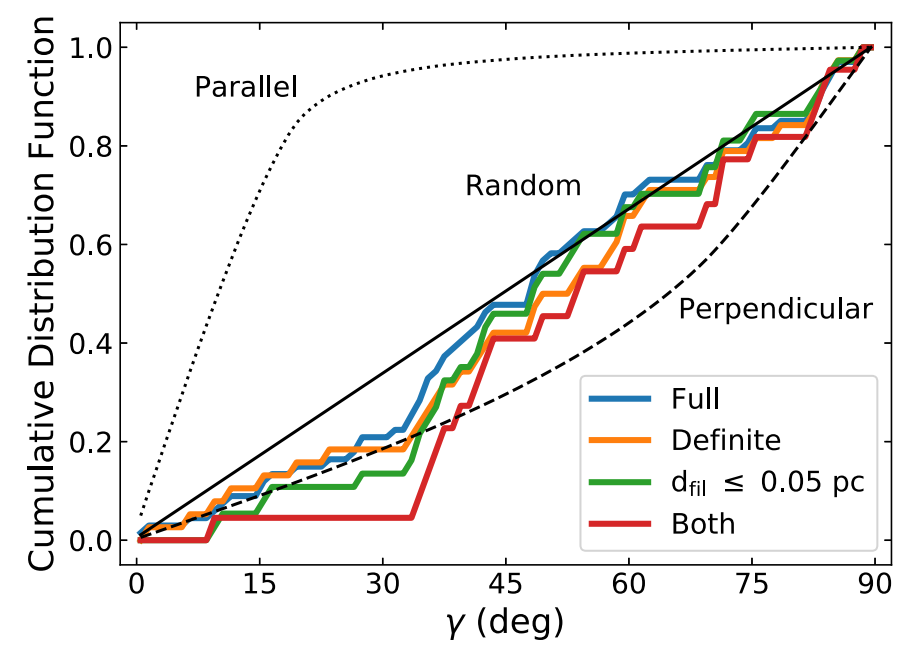


Figure 11. Cumulative distribution of projected angle between outflows and filaments. Colored lines show the distribution of  $\gamma$  for different subsets of our outflow catalog. Black lines show the expected distribution given three different model distributions. Parallel case contains only 3D angles between  $0^{\circ}$  and  $20^{\circ}$ , the random case contains all 3D angles between  $0^{\circ}$  and  $90^{\circ}$ , and the perpendicular case contains 3D angles between  $70^{\circ}$  and  $90^{\circ}$ . Results of Anderson–Darling tests between the observed and modeled distributions are in Table 4 (see Section 5.2).

In particular, the "Both" subsample with the 22 definite outflow lobes closest to their filaments contains only one lobe with  $\gamma < 33^{\circ}$ , compared to the  $\sim 8$  that would be expected if  $\gamma$  were distributed randomly.

While Figure 11 shows that the "Parallel" scenario is clearly inconsistent with the observed distribution of  $\gamma$ , the "Perpendicular" distribution is more difficult to rule out. We apply the Anderson–Darling (AD) test (Stephens 1974) to determine if the perpendicular or random distributions can be rejected for each outflow subsample. The AD p-values listed in Table 4 represent the likelihood that the observed outflow-filament  $\gamma$  distribution is drawn from either the random or perpendicular distribution. We do not report the results of AD tests for the parallel case; the p-values for the parallel distribution are all close to zero.

Based on the AD test, we reject the hypothesis that the full outflow sample is drawn from a perpendicular distribution with >99.9% confidence (p < 0.001), while the random distribution is not ruled out. The results are similar for the definite subsample, though we can only rule out the perpendicular distribution with 94% confidence (p = 0.06). For the  $d_{\rm fil} \le 0.05\,{\rm pc}$  subsample, we can rule out the perpendicular distribution with 98% confidence (p = 0.02). Though these subsamples are unlikely to be drawn from a purely perpendicular distribution, their p-values are higher than the equivalent in Stephens et al. (2017). We do not test models with a mixture of perpendicular and parallel outflow-filament alignment, but such a bimodal distribution may be a better fit to our data than either the random or perpendicular model alone.

If we limit the sample to the definite outflows with  $d_{\rm fil} \leqslant 0.05\,{\rm pc}$  ("Both") and compare to the perpendicular model, we calculate an AD p-value of >0.25. While we cannot rule out with better than 94% confidence (p=0.06) that this subsample of outflows is drawn from a random distribution, the perpendicular model more closely matches the angular

**Table 4** Anderson–Darling *p*-values

Sample	Random	Perpendicular
Full	0.23	>0.001
Definite	>0.25	0.06
$d_{\rm fil} \leqslant 0.05~{ m pc}$	0.13	0.02
Both	0.06	>0.25
Stephens et al. (2017) <sup>a</sup>	0.20	0.0045
Kong et al. (2019) b	$6.5 \times 10^{-5}$	0.53

#### Notes.

distribution of these close outflow-filament pairs. We tentatively conclude that the clearest outflow-filament pairs in Orion A are perpendicularly aligned.

In Perseus, Stephens et al. (2017) found a random distribution of outflow-filament angles. This random alignment could reflect processes at large or small scales. At large scales, the orientation of filaments may be irrelevant to the accretion of mass onto them, contradicting simulations of filament formation (e.g., Chen & Ostriker 2014; Clarke et al. 2017). At core scales, no matter the orientation of mass accretion, the protostellar angular momentum may be randomized by multiplicity or turbulence, as seen in simulations by Offner et al. (2016) and Lee et al. (2017). Our finding of a moderately perpendicular alignment between outflows and filaments in Orion A may mean that filament formation or protostellar mass accretion is different in Perseus and Orion.

In the IRDC G28, Kong et al. (2019) found a remarkably perpendicular outflow-filament alignment, rejecting a random distribution at high confidence (see Table 4). Such a strong perpendicular alignment is predicted in simulations of IRDCs

<sup>&</sup>lt;sup>a</sup> Perseus outflows;  $\gamma_{\rm F}$  in their Table 3.

<sup>&</sup>lt;sup>b</sup> IRDC G28 outflows.

by Li et al. (2018) and Li & Klein (2019), resulting from filament formation perpendicular to a strong magnetic field and continuous mass accretion along the magnetic field lines onto protostellar cores. As IRDCs are generally considered to be in the earliest phase of massive star formation (Rathborne et al. 2006), the outflow-filament alignment may be related to evolutionary stage or magnetic field. A comprehensive study of outflow-filament alignment across many different star-forming environments is necessary to answer this question.

While we find some evidence for perpendicular outflow-filament alignment in Orion A, previous studies have concluded that outflows and filaments in this cloud are randomly aligned. Davis et al. (2009) show that the position angles of  $H_2$  jets in Orion A are distributed uniformly and oriented randomly with respect to the  $\sim$ pc-scale integral-shaped filament. Tanabe et al. (2019) conclude the same using their CO outflow catalog. Our study is not directly comparable to these, as we use the  $C^{18}O$  filaments, which reveal the integral-shaped filament to be made up of many smaller filamentary structures.

The moderately perpendicular outflow-filament alignment may also be a result of observational biases. If we preferentially miss outflows that are parallel to their filaments, this could bias the outflow-filament alignment. An outflow launched parallel to its host filament will encounter more dense gas than a perpendicularly launched outflow. Thus, parallel outflows may be smaller or slower and consequently harder to detect; this effect is seen in the simulations of Offner et al. (2011). If this bias is present, we would expect to detect more parallel outflows with higher-resolution observations. The physical resolution of the Perseus observations used by Stephens et al. (2017) is about  $4 \times$  better than the CARMA-NRO Orion A survey used here. This could help explain the deficit of parallel outflows seen in Orion relative to Perseus. The Kong et al. (2019) IRDC observations have a physical resolution similar to that of our data, so this observational bias cannot explain the difference between the outflow-filament alignment in the IRDC and Orion.

# 6. Conclusions

We have identified 45 outflows in the CARMA–NRO Orion CO maps of Orion A. Eleven of these outflows are new detections. For the previously known outflows, we improve the earlier estimates of their mass by including a correction for low-velocity mass as well as a velocity-dependent opacity correction. The outflows contain significant momentum and kinetic energy compared to estimates for the turbulent dissipation in Orion A. If outflows couple efficiently to the cloud, they can maintain cloud turbulence and slow star formation. There is still considerable uncertainty in the outflow impact, and a mechanism for transporting momentum from the outflow length scale to the larger cloud is needed; see Offner & Liu (2018) for one such option.

We compare the outflow position angles to the orientation of nearby filaments from the C<sup>18</sup>O catalog of Suri et al. (2019). The full outflow catalog is consistent with random outflow-filament alignment. The most reliable outflows that are closest to their filaments show a moderately perpendicular outflow-filament alignment.

While we improve the specificity of the outflow-filament comparison compared to previous studies of Orion A by using the C<sup>18</sup>O filament catalog, there is still uncertainty in pairing outflows and filaments. Future work should investigate the outflow-filament alignment over multiple length scales and take into account the varying filament width.

The outflow-filament alignment may change as protostars evolve. A detailed comparison should be made between this alignment and protostellar properties such as bolometric temperature, multiplicity, and evolutionary stage. A combination of this sample with the studies in other clouds could provide enough statistical power to answer these more specific questions about outflow-filament alignment and the mass assembly of protostars.

We are grateful to the referee, Neal Evans, for his valuable suggestions, as well as to Ian Stephens, Cheng-Han Hsieh, and the CARMA–NRO Orion collaboration for discussions that improved this study.

CARMA operations were supported by the California Institute of Technology, the University of California-Berkeley, the University of Illinois at Urbana-Champaign, the University of Maryland College Park, and the University of Chicago. The Nobeyama 45 m telescope is operated by the Nobeyama Radio Observatory, a branch of the National Astronomical Observatory of Japan. J.R.F, H.G.A., and S.K. were funded by the National Science Foundation awards AST-1140063 and AST-1714710.

Facilities: CARMA, No:45 m, CDS.

Software: Astropy (Astropy Collaboration et al. 2013), spectral-cube (Robitaille et al. 2016).

# Appendix A Protostellar Properties

The HOPS catalog from Furlan et al. (2016) compiles photometric measurements for protostars from 1.2 to 870  $\mu$ m. From these SEDs, they calculate the bolometric luminosity  $L_{\text{bol}}$ and temperature  $T_{\text{bol}}$ . The value of  $L_{\text{bol}}$  is calculated by integrating the observed SED directly. If dominated by accretion luminosity,  $L_{bol}$  is a function of the accretion rate and protostellar mass (Takahashi et al. 2008). Since accretion adds mass to the protostar,  $L_{bol}$  may be considered a proxy for the protostellar mass. Here,  $T_{\rm bol}$  is the temperature of a blackbody with the same mean frequency as the observed SED. The value of  $T_{\text{bol}}$  increases as a protostar evolves and clears its envelope, making it a proxy for protostellar age (Myers & Ladd 1993). While  $L_{\text{bol}}$  and  $T_{\text{bol}}$  are generally thought to trace the protostellar mass and age, respectively, other factors such as extinction and inclination may also affect these measurements. For the 40 outflows presented here with associated HOPS sources, we show the correlation between the protostellar  $L_{\text{bol}}$  and  $T_{\text{bol}}$  and outflow properties in Figure A1. Arce & Sargent (2006) discovered a correlation between outflow opening angle and protostellar age, as traced by  $T_{\rm bol}$ . They found that more evolved (hotter  $T_{\text{bol}}$ ) protostars drive wider outflows. Figure A1 shows that our measured outflow opening angles are not correlated with  $T_{\text{bol}}$  or  $L_{\text{bol}}$ .

Takahashi et al. (2008) investigated the relationship between momentum flux (identical to our  $\dot{P}$ ) and  $L_{\text{bol}}$  in the outflows

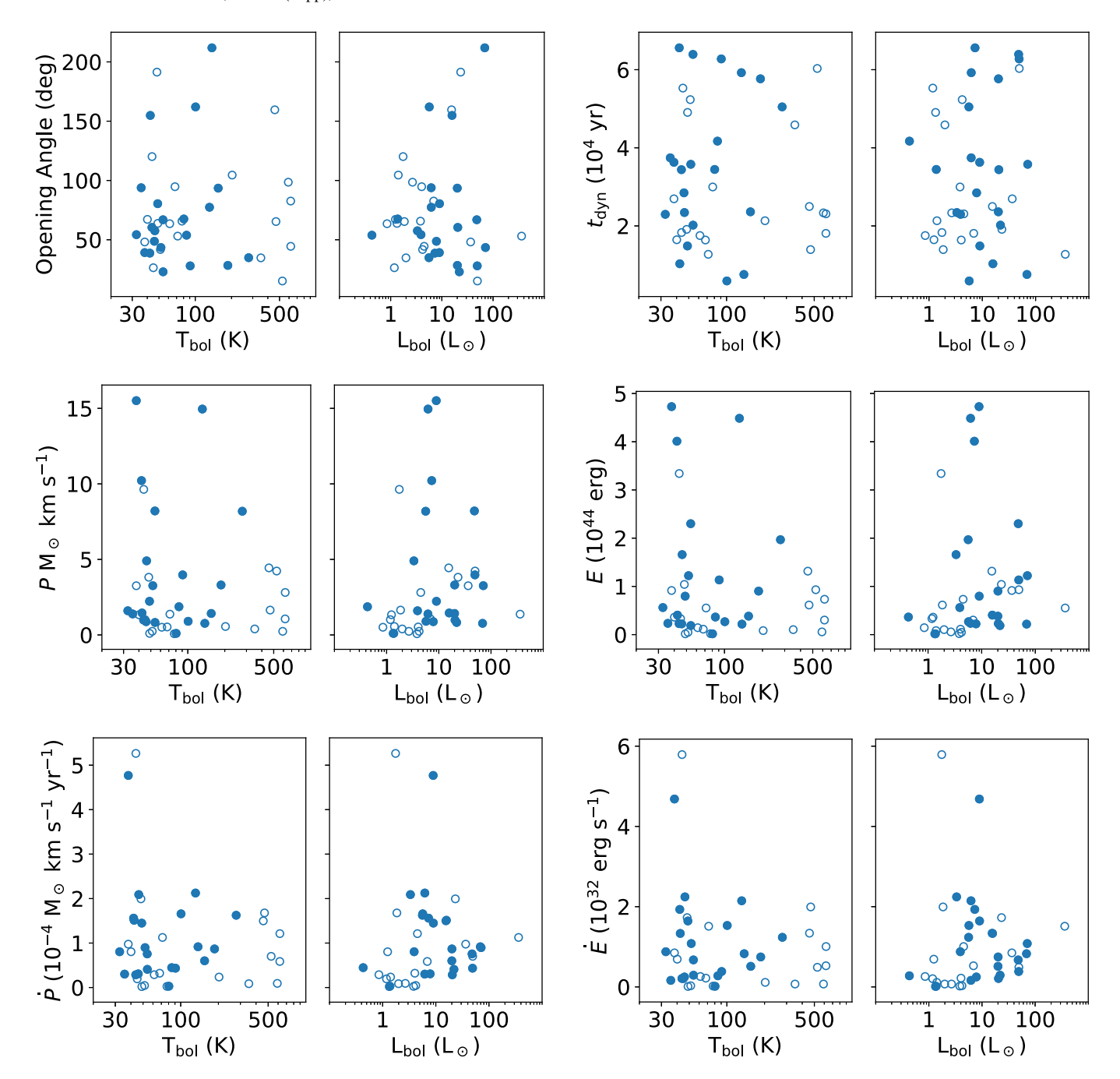


Figure A1. Protostellar  $T_{\rm bol}$  and  $L_{\rm bol}$  plotted against outflow properties for 40 outflows driven by HOPS sources. Outflow properties are the average of both lobes, when detected. Filled circles indicate outflows with a confidence level of "definite" for all detected lobes. Open circles indicate outflows with at least one "marginal" lobe. Outflow properties are given in Tables 2 and 3.

they identified in OMC-2/3. In their Figure A1, they show these outflows to be consistent with a trend of increasing  $\dot{P}$  with increasing  $L_{\rm bol}$  spanning six orders of magnitude in  $L_{\rm bol}$ . As shown in Figure A1, we find no evidence for a correlation between  $\dot{P}$  and  $L_{\rm bol}$  within our outflow sample. However, our measurements are consistent with the scatter seen in Figure 12 of Takahashi et al. (2008). Figure A1 also shows the lack of

correlation between the protostellar  $T_{\rm bol}$  or  $L_{\rm bol}$  with the outflow momentum P, kinetic energy E, energy injection rate  $\dot{E}$ , and dynamical time  $t_{\rm dyn}$ .

We also look for any difference in the outflow-filament alignment as a function of protostellar  $T_{\rm bol}$  and  $L_{\rm bol}$ . In Perseus, older, less embedded, hotter  $T_{\rm bol}$  protostars show a slightly more perpendicular outflow-filament alignment than younger

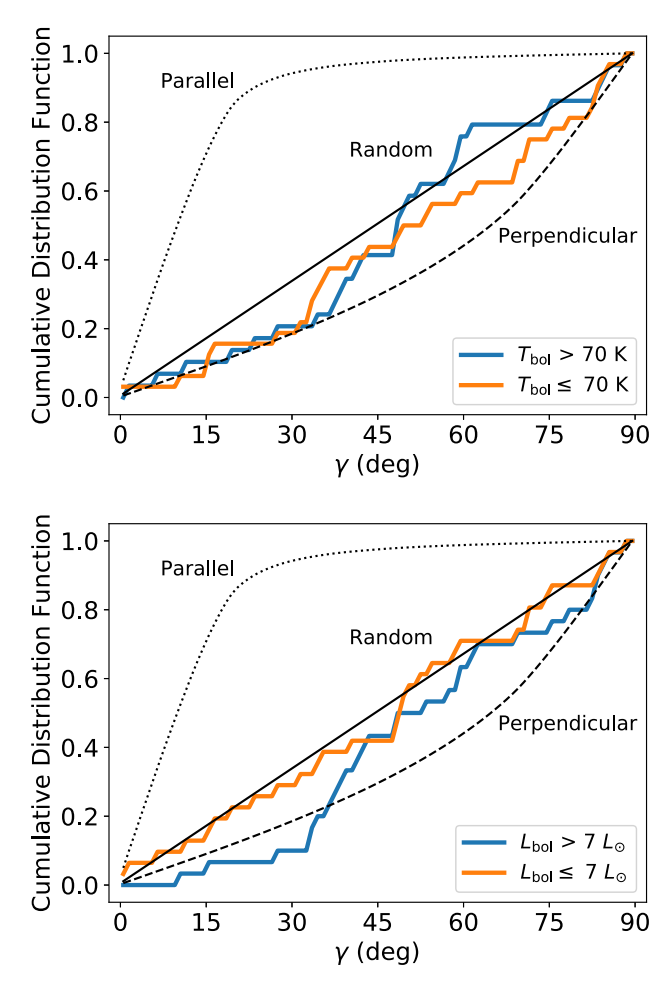


Figure A2. Outflow-filament alignment in samples with low and high  $T_{\rm bol}$  and  $L_{\rm bol}$ . Symbols are the same as Figure 11.

protostars (Stephens et al. 2017). In Figure A2, we show the outflow-filament alignment in Orion A among HOPS protostars, split into samples with low and high values for  $T_{\rm bol}$  and  $L_{\rm bol}$ . There is no significant difference between the low- and high- $T_{\rm bol}$  outflow-filament alignment. The high- $L_{\rm bol}$  outflows

are slightly more consistent with a perpendicular outflow-filament alignment, compared to the low- $L_{\rm bol}$  sample.

# Appendix B All Outflows in CARMA-NRO Orion

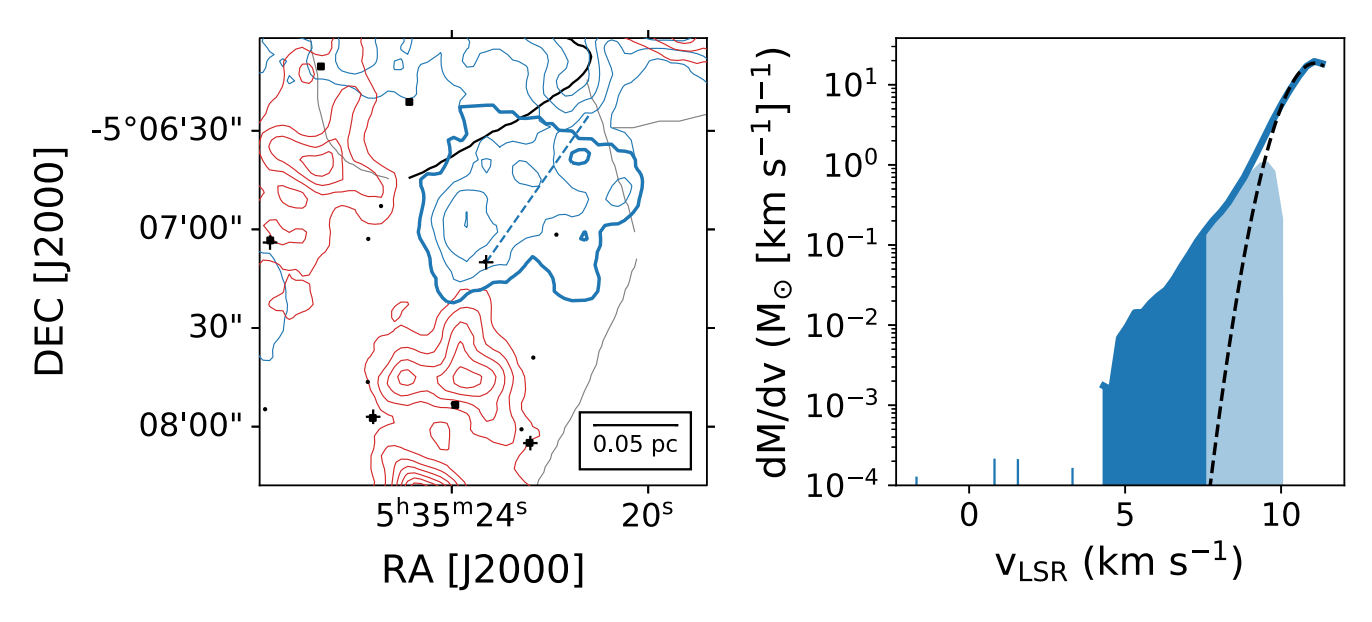


Figure B1. SMZ 11 outflow. Left panel shows the outflow, position angle, nearby sources, and filaments. The velocity range of integration is given by  $v_{blue}/v_{red}$  in Table 1 and the contours go from 5 to  $50\sigma$  in steps of  $5\sigma$ , where  $\sigma$  is the rms error in the integrated map. Symbols are the same as Figure 2. Right panel shows the mass spectrum with fit, where  $\sigma$  is the rms error in the integrated map. Symbols are the same as Figure 6. The complete figure set (45 images) is available in the online journal.

(The complete figure set (45 images) is available.)

#### **ORCID iDs**

Jesse R. Feddersen https://orcid.org/0000-0003-3810-3323 Héctor G. Arce https://orcid.org/0000-0001-5653-7817 Shuo Kong https://orcid.org/0000-0002-8469-2029 Volker Ossenkopf-Okada https://orcid.org/0000-0002-8351-3877

Michael M. Dunham https://orcid.org/0000-0003-0749-9505 Fumitaka Nakamura https://orcid.org/0000-0001-5431-2294 Yoshito Shimajiri https://orcid.org/0000-0001-9368-3143 John Bally https://orcid.org/0000-0001-8135-6612

```
References
Anathpindika, S., & Whitworth, A. P. 2008, A&A, 487, 605
André, P., Di Francesco, J., Ward-Thompson, D., et al. 2014, in Protostars and
  Planets VI, ed. H. Beuther et al. (Tucson, AZ: Univ. Arizona Press), 27
Arce, H. G., Borkin, M. A., Goodman, A. A., Pineda, J. E., & Halle, M. W.
   2010, ApJ, 715, 1170
Arce, H. G., & Goodman, A. A. 2001a, ApJ, 554, 132
Arce, H. G., & Goodman, A. A. 2001b, ApJL, 551, L171
Arce, H. G., & Sargent, A. I. 2006, ApJ, 646, 1070
Arce, H. G., Shepherd, D., Gueth, F., et al. 2007, in Protostars and Planets V,
   ed. B. Reipurth, D. Jewitt, & K. Keil (Tucson, AZ: Univ. Arizona
   Press), 245
Arzoumanian, D., André, P., Didelon, P., et al. 2011, A&A, 529, L6
Aso, Y., Tatematsu, K., Sekimoto, Y., et al. 2000, ApJS, 131, 465
Astropy Collaboration, Robitaille, T. P., Tollerud, E. J., et al. 2013, A&A,
  558, A33
Bally, J. 2016, ARA&A, 54, 491
Bally, J., Ginsburg, A., Arce, H., et al. 2017, ApJ, 837, 60
Bally, J., Langer, W. D., Stark, A. A., & Wilson, R. W. 1987, ApJL, 312, L45
Berné, O., Marcelino, N., & Cernicharo, J. 2014, ApJ, 795, 13
Bodenheimer, P. 1995, ARA&A, 33, 199
Brunt, C. M., Heyer, M. H., & Mac Low, M. M. 2009, A&A, 504, 883
Buckle, J. V., Davis, C. J., Francesco, J. D., et al. 2012, MNRAS, 422, 521
Carroll, J. J., Frank, A., & Blackman, E. G. 2010, ApJ, 722, 145
Carroll, J. J., Frank, A., Blackman, E. G., Cunningham, A. J., & Quillen, A. C.
   2009, ApJ, 695, 1376
Chen, C.-Y., & Ostriker, E. C. 2014, ApJ, 785, 69
```

```
Chernin, L. M., & Masson, C. R. 1995, ApJ, 455, 182
Chini, R., Reipurth, B., Ward-Thompson, D., et al. 1997, ApJL, 474, L135
Choi, M., Kang, M., Lee, J.-E., et al. 2017, ApJS, 232, 24
Clarke, S. D., Whitworth, A. P., Duarte-Cabral, A., & Hubber, D. A. 2017,
   MNRAS, 468, 2489
Curtis, E. I., Richer, J. S., Swift, J. J., & Williams, J. P. 2010, MNRAS,
  408, 1516
Davis, C. J., Dent, W. R. F., Matthews, H. E., Coulson, I. M., &
  McCaughrean, M. J. 2000, MNRAS, 318, 952
Davis, C. J., Froebrich, D., Stanke, T., et al. 2009, A&A, 496, 153
Downes, T. P., & Cabrit, S. 2007, A&A, 471, 873
Dunham, M. M., Arce, H. G., Mardones, D., et al. 2014, ApJ, 783, 29
Feddersen, J. R., Arce, H. G., Kong, S., et al. 2018, ApJ, 862, 121
Federrath, C. 2015, MNRAS, 450, 4035
Frank, A., Ray, T. P., Cabrit, S., et al. 2014, in Protostars and Planets VI, ed.
  H. Beuther et al. (Tucson, AZ: Univ. Arizona Press), 451
Frerking, M. A., Langer, W. D., & Wilson, R. W. 1982, ApJ, 262, 590
Furlan, E., Fischer, W. J., Ali, B., et al. 2016, ApJS, 224, 5
Goldsmith, P. F., Snell, R. L., Hemeon-Heyer, M., & Langer, W. D. 1984, ApJ,
Großschedl, J. E., Alves, J., Meingast, S., et al. 2018, A&A, 619, A106
Hacar, A., Tafalla, M., Kauffmann, J., & Kovács, A. 2013, A&A, 554, A55
Kauffmann, J., Bertoldi, F., Bourke, T. L., Evans, N. J. I., & Lee, C. W. 2008,
Koch, E. W., & Rosolowsky, E. W. 2015, MNRAS, 452, 3435
Kong, S., Arce, H. G., Feddersen, J. R., et al. 2018, ApJS, 236, 25
Kong, S., Arce, H. G., José Maureira, M., et al. 2019, ApJ, 874, 104
Konigl, A., & Pudritz, R. E. 2000, in Protostars and Planets IV, ed.
   V. Mannings, A. P. Boss, & S. S. Russell (Tucson, AZ: Univ. Arizona
Kounkel, M., Covey, K., Suárez, G., et al. 2018, AJ, 156, 84
Kuhn, M. A., Hillenbrand, L. A., Sills, A., Feigelson, E. D., & Getman, K. V.
  2019, ApJ, 870, 32
Langer, W. D., & Penzias, A. A. 1993, ApJ, 408, 539
Lee, J. W. Y., Hull, C. L. H., & Offner, S. S. R. 2017, ApJ, 834, 201
Li, H., Li, D., Qian, L., et al. 2015, ApJS, 219, 20
Li, P. S., & Klein, R. I. 2019, MNRAS, 485, 4509
Li, P. S., Klein, R. I., & McKee, C. F. 2018, MNRAS, 473, 4220
McKee, C. F., & Ostriker, E. C. 2007, ARA&A, 45, 565
Megeath, S. T., Gutermuth, R., Muzerolle, J., et al. 2012, AJ, 144, 192
Meingast, S., Alves, J., Mardones, D., et al. 2016, A&A, 587, A153
Menten, K. M., Reid, M. J., Forbrich, J., & Brunthaler, A. 2007, A&A,
  474, 515
```

```
Morgan, J. A., Schloerb, F. P., Snell, R. L., & Bally, J. 1991, ApJ, 376, 618
Moro-Martín, A., Cernicharo, J., Noriega-Crespo, A., & Martín-Pintado, J.
   1999, ApJL, 520, L111
Myers, P. C., & Ladd, E. F. 1993, ApJL, 413, L47
Nakamura, F., Kamada, Y., Kamazaki, T., et al. 2011, ApJ, 726, 46
Nakamura, F., & Li, Z.-Y. 2007, ApJ, 662, 395
Nakamura, F., Miura, T., Kitamura, Y., et al. 2012, ApJ, 746, 25
Offner, S. S. R., Dunham, M. M., Lee, K. I., Arce, H. G., & Fielding, D. B.
   2016, ApJL, 827, L11
Offner, S. S. R., Lee, E. J., Goodman, A. A., & Arce, H. 2011, ApJ, 743, 91
Offner, S. S. R., & Liu, Y. 2018, NatAs, 2, 896
Padoan, P., Juvela, M., Kritsuk, A., & Norman, M. L. 2009, ApJL, 707, L153
Plunkett, A. L., Arce, H. G., Corder, S. A., et al. 2013, ApJ, 774, 22
Plunkett, A. L., Arce, H. G., Corder, S. A., et al. 2015, ApJ, 803, 22
Rathborne, J. M., Jackson, J. M., & Simon, R. 2006, ApJ, 641, 389
Ripple, F., Heyer, M. H., Gutermuth, R., Snell, R. L., & Brunt, C. M. 2013,
```

- MNRAS, 431, 1296
  Robitaille, T., Ginsburg, A., Beaumont, C., Leroy, A., & Rosolowsky, E. 2016, Spectral-cube: Read and Analyze Astrophysical Spectral Data Cubes, Astrophysics Source Code Library, ascl:1609.017
- Rohlfs, K., & Wilson, T. L. 1996, Tools of Radio Astronomy (Berlin: Springer), 127
- Schmid-Burgk, J., Guesten, R., Mauersberger, R., Schulz, A., & Wilson, T. L. 1990, ApJL, 362, L25

```
    Shimajiri, Y., Kawabe, R., Takakuwa, S., et al. 2011, PASJ, 63, 105
    Shimajiri, Y., Takahashi, S., Takakuwa, S., Saito, M., & Kawabe, R. 2008, ApJ, 683, 255
```

- Shimajiri, Y., Takahashi, S., Takakuwa, S., Saito, M., & Kawabe, R. 2009, PASJ, 61, 1055
- Shu, F. H., Najita, J. R., Shang, H., & Li, Z. Y. 2000, in Protostars and Planets IV, ed. V. Mannings, A. P. Boss, & S. S. Russell (Tucson, AZ: Univ. Arizona Press), 789
- Sousbie, T. 2011, MNRAS, 414, 350
- Stanke, T., McCaughrean, M. J., & Zinnecker, H. 2002, A&A, 392, 239 Stanke, T., & Williams, J. P. 2007, AJ, 133, 1307
- Stephens, I. W., Dunham, M. M., Myers, P. C., et al. 2017, ApJ, 846, 16
- Stephens, M. A. 1974, Journal of the American Statistical Association, 69, 730 Suri, S., Sánchez-Monge, Á, Schilke, P., et al. 2019, A&A, 623, A142
- Takahashi, S., Saito, M., Ohashi, N., et al. 2008, ApJ, 688, 344
- Tanabe, Y., Nakamura, F., Tsukagoshi, T., et al. 2019, PASJ, 71, 8
  Teixeira, P. S., Takahashi, S., Zapata, L. A., & Ho, P. T. P. 2016, A&A, 587, A47
- Williams, J. P., Plambeck, R. L., & Heyer, M. H. 2003, ApJ, 591, 1025
  Wilson, B. A., Dame, T. M., Masheder, M. R. W., & Thaddeus, P. 2005, A&A, 430, 523
- Yang, Y.-L., Green, J. D., Evans, N. J., II, et al. 2018, ApJ, 860, 174 Zapata, L. A., Rodríguez, L. F., Ho, P. T. P., et al. 2005, ApJL, 630, L85 Zhang, Y., Arce, H. G., Mardones, D., et al. 2016, ApJ, 832, 158